

Changes in Jupiter's Great Red Spot (1979–2006) and Oval BA (2000–2006)

Sushil Shetty*, Philip S. Marcus

Department of Mechanical Engineering, University of California, Berkeley, CA 94720, USA

ARTICLE INFO

Article history:

Received 13 September 2009

Revised 18 June 2010

Accepted 18 June 2010

Available online 1 July 2010

Keywords:

Jupiter, Atmosphere
Atmospheres, Dynamics
Atmospheres, Evolution

ABSTRACT

We analyze velocity fields of the Great Red Spot (GRS) and Oval BA that were previously extracted from Cassini, Galileo, and Hubble Space Telescope images (Asay-Davis, X.S., Marcus, P.S., Wong, M., de Pater, I. [2009]. *Icarus* 203, 164–188). Our analyses use reduced-parameter models in which the GRS, Oval BA, and surrounding zonal (east–west) flows are assumed to have piece-wise-constant potential vorticity (PV), but with finite-sized transition regions between the pieces of constant PV rather than sharp steps. The shapes of the regions of constant PV are computed such that the flow is a steady, equilibrium solution of the 2D quasigeostrophic equations when viewed in a frame translating uniformly in the east–west direction. All parameter values of the models, including the magnitudes of the PV, areas of the regions with constant PV, locations of the transition regions, widths of the transition regions, and the value of the Rossby deformation radius, are found with a genetic algorithm such that the velocity produced by the equilibrium solution is a “best-fit” to the observed velocity fields. A Monte Carlo method is used to estimate the uncertainties in the best-fit parameter values.

The best-fit results show that there were significant changes (greater than the uncertainties) in the PV of the GRS between Galileo in 1996 and Hubble in 2006. In particular, the shape of the PV anomaly of the GRS became rounder, and the area of the PV anomaly of the GRS decreased by 18%, although the magnitudes of PV in the anomaly remained constant. In contrast, neither the area nor the magnitude of the PV anomaly of the Oval BA changed from 2000, when its cloud cover was white, to 2006, when its cloud cover was red. The best-fit results also show that the areas of the PV anomalies of the GRS and of the Oval BA are smaller than the areas of their corresponding cloud covers at all times. Using the best-fit values of the Rossby deformation radius, we show that the Brunt–Väisälä frequency is 15% larger at 33°S than at 23°S. As expected (Marcus, 1993), the best-fit results show that the PV of the zonal flow has “jumps” at the latitudes of the maxima of the eastward-going jet streams. However, a surprising result is that a large “jump” in the PV of the zonal flow occurs at the location of a maximum of the westward going jet stream neighboring the GRS. Another surprise is that the jumps in the PV of the zonal flow do not all have the same sign, which implies that there is not a monotonic “staircase” of zonal PV from north to south as was anticipated (Marcus, 1993; McIntyre, 2008).

© 2010 Elsevier Inc. All rights reserved.

1. Introduction

Some jovian features can be measured directly from satellite images or the velocity fields derived from them, such as the magnitudes and locations of the peak velocities of the winds (Asay-Davis et al., 2009) of the Great Red Spot (GRS) and the area (Simon-Miller et al., 2002) of the clouds associated with the GRS. However properties such as the atmosphere's vertical stratification must be inferred indirectly by modeling and solving an “inverse problem”. Often, the latter is done by computing solutions of an initial-value problem that consists of (1) a model set of equations that approximates the atmosphere's dynamics, (2) a set of unknown parameters that describe the mean properties of the atmosphere, such as the vertical stratification, and (3) a set of initial conditions. The values of the unknown parameters and initial con-

ditions are varied until the computed solution “best-fits” the observations. Most inverse studies of the jovian atmosphere (Dowling and Ingersoll, 1989; Cho et al., 2001; Morales-Juberías et al., 2003; Morales-Juberías and Dowling, 2005; García-Melendo et al., 2007; Legarreta and Sánchez-Lavega, 2008), use initial-value codes and have a dozen, or so, free parameter values for which “best-fit” values are sought.¹ For a model with 11 free parameters,

¹ In an initial-value code, in addition to the free parameters of the model, there are also the choices of initial condition. In principle, for conservative codes, the number of free parameters associated with the initial conditions is equal to the number of spatial resolution elements of the code (e.g., grid points). However, since most initial-value codes are dissipative either explicitly or implicitly by grid dissipation, there are basins of attraction associated with the initial conditions. Thus, the effective number of independent free parameters of the initial condition is far fewer than the number of resolution elements and difficult to quantify. This dissipation leads to another disquieting aspect of using an initial-value code in a search for best-fit models. Because the areas and magnitude of the PV of a vortex change as the flow evolves, those values in the final flow often differ from those of the initial flow, making it difficult to choose initial conditions that sample the parameter space without bias.

* Corresponding author. Current address: Schlumberger-Doll Research, 1 Hampshire Street, Cambridge, MA 02139, USA.

E-mail address: sushilshetty@gmail.com (S. Shetty).

such as the one used in this study, finding the “best-fit” values by sampling just 3 values of each parameter would require 177,147 trials of the initial-value code; whereas previous published studies with 11 or so parameters use fewer than 100 trials. The reason for so few trials is due to the computational expense of initial-value codes, which usually take tens of thousands of time steps (with wall-clock times on the order of days) to converge to an approximately steady or self-similar solution for a high spatial resolution code. To find the “best-fit” parameters with only 100 trials requires intuition (or luck), i.e., finding that the results are nearly independent of some parameter combinations and highly sensitive to others (cf., Shetty et al., 2007). In Shetty et al. (2007) we applied inverse methods to the GRS using a “trait-matching” method with velocity fields extracted from Voyager mosaics to solve the inverse problem. We found that some properties (i.e., “traits”) of the GRS were sensitive to the values of some parameters and nearly independent of others, and defined the model’s “best-fit” values as those the best reproduced the traits. Although this method was computationally economical, there were limitations: (1) Although “trait-matching” can be applied to other jovian vortices, there is no systematic method of extending it to find the parameter values of other jovian features, such as stagnation points. (2) We were able to carry out a *sensitivity* analysis of the derived parameters, (i.e., we determined how a model velocity field changes as a function of small changes in the model parameter values). However, we did not carry out an *uncertainty* analysis of the derived parameters because we felt that the poor quality and lack of published uncertainties of the velocity vectors of the GRS that we used in that study did not warrant a more thorough and time-consuming analysis. The velocity vectors used in the “trait-matching” study were manually-derived from the Voyager images and were very sparse. (3) In our “trait-matching” study, we did not have a systematic way of sampling the parameter space to find the “best-fit” values. (4) Two of the key parameters of the “trait-matching” model were determined by using the peak magnitudes of the observed velocities along the GRS’s east–west principal axes. However, *all* methods for extracting the value of the local maxima of velocity fields from cloud images systematically underestimate peak magnitudes (Asay-Davis et al., 2009), which suggests that traits that depend on peak magnitudes should not be used. (5) Using “trait-matching”, we discovered several degenerate couplings; for example, the value of the peak velocities in the high-speed collar of the GRS was only sensitive to the *product* of the values of two of the unknown parameters for which we were seeking best-fit values. Thus, we found that we could vary the value of one of the parameters over a wide range, and as long as we chose the value of the other parameter so that the product had the correct value, we obtained the observed velocity field in the collar. Thus, without additional constraints on one or both of the parameter values, it would have been impossible to find their values. (6) Because the traits used in the matching depended upon relatively few of the observed velocity vectors, we were unable to exploit most of the observations to find the “best-fit” parameter values.

To address the shortcomings of the trait-matching method, in this paper we solve the inverse problem using a new method that uses *all* of the velocity vectors in a field containing a jovian feature, rather than just those few that are part of the trait. Instead of using an initial-value code to compute solutions, we use a “fast-solver”, that is, a numerical algorithm that computes steady-state (as observed in a frame translating with the vortex) solutions to the equations of motion by an iterative method. Using a fast-solver, which finds equilibria in 20–30 iterations (with wall-clock times on the order of minutes), we can compute quickly tens of thousands, rather than a hundred, steady-state solutions with different parameter values. We use a genetic algorithm (see Appendix) to find systematically the “best-fit” parameters to the observed (extracted) velocity fields by minimizing a cost-function. The algo-

ri thm allows us to search parameter space for “best-fit” values, so that we can, for example, find best-fit values for 11 parameters with on the order of 10,000 trials rather than 200,000. The cost-functions we chose (see Section 3.2) uses the uncertainties of the observed velocity vectors. For this reason, our input velocity fields were created with Advection Corrected Correlation Image Velocimetry (ACCIV) (Asay-Davis et al., 2009) or Correlation Image Velocimetry (CIV) (Fincham et al., 1997), which are automated velocity-extraction algorithms that not only extracts the velocities but also their uncertainties. The fields created with ACCIV of the GRS and Oval BA have tens to hundreds of thousands of *independent* velocity vectors with uncertainties on the order of 5 m s^{-1} .

The goal of this study is to use velocity fields extracted between 1996 and 2006 from images from Galileo, Cassini, and the Hubble Space Telescope (HST), to determine the best-fit parameter values for this model and to see how they vary over time. To conclude that a parameter value changed in time, it is necessary to show that the measured change is greater than the uncertainties of the derived parameter values. For this reason we include an analysis of those uncertainties using a Monte Carlo method (cf., Press et al., 1988).

The remainder of the paper is organized as follows. In Section 2, we list the ACCIV-extracted velocity fields used in this study and review their uncertainties. In Section 3 we review the equations of motion, list all of the parameters for which we seek best-fit values and outline the difference between solving the inverse problem with an initial-value code and with a steady-state finding code. In Section 4, we present the results of our search for best-fit parameter values and their uncertainties for the GRS and Oval BA and their neighboring jet streams. In Sections 5 and 6 we provide physical explanations of the parameter values and discuss their temporal changes for the GRS and Oval BA, respectively. Limitations of the model are discussed in Section 7 and our conclusions are in Section 8.

2. Observations

2.1. Velocities and uncertainties

For the analyses in this paper, we use velocity fields of the GRS (Fig. 1) and Oval BA (Fig. 2) between 1996 and 2006 that were extracted using images from Galileo, Cassini, and HST. Details of the velocity extraction are in Asay-Davis et al. (2009). The properties of the fields are summarized in Table 1. We do not include velocity fields that were manually extracted from the 1979 Voyager mosaics because they do not have uncertainties for the extracted velocities, and the velocity fields are sparse, containing approximately 1000 vectors (Fig. 3), making it difficult to interpolate accurately from the vector locations to grid points. Table 1 lists the ACCIV *correlation uncertainties* (defined in Appendix) of the extracted velocity vectors. Using a synthetic velocity field, Asay-Davis et al. (2009) showed that the correlation uncertainty is a good measure at each location of the actual error between the real velocity and the extracted velocity. Because the correlation uncertainty is expensive to compute, we use the *scatter uncertainties* of the extracted velocities (see Appendix for the definition) for all analyses in this paper. Analysis of synthetic velocity fields shows that the actual errors can be up to twice as large as the scatter uncertainties. Table 1 shows that the RMS average of all of the correlation uncertainties of all of the velocities that were extracted from the HST observations of the GRS is 5 m s^{-1} .

In addition to the velocities of the vortices themselves, to analyze the GRS and Oval BA it is also necessary to have either the velocity of the atmosphere at the latitudes of the vortices at *all* longitudes, or to make assumptions about that flow. It is commonly assumed that the flow far from the Oval and GRS is steady in time

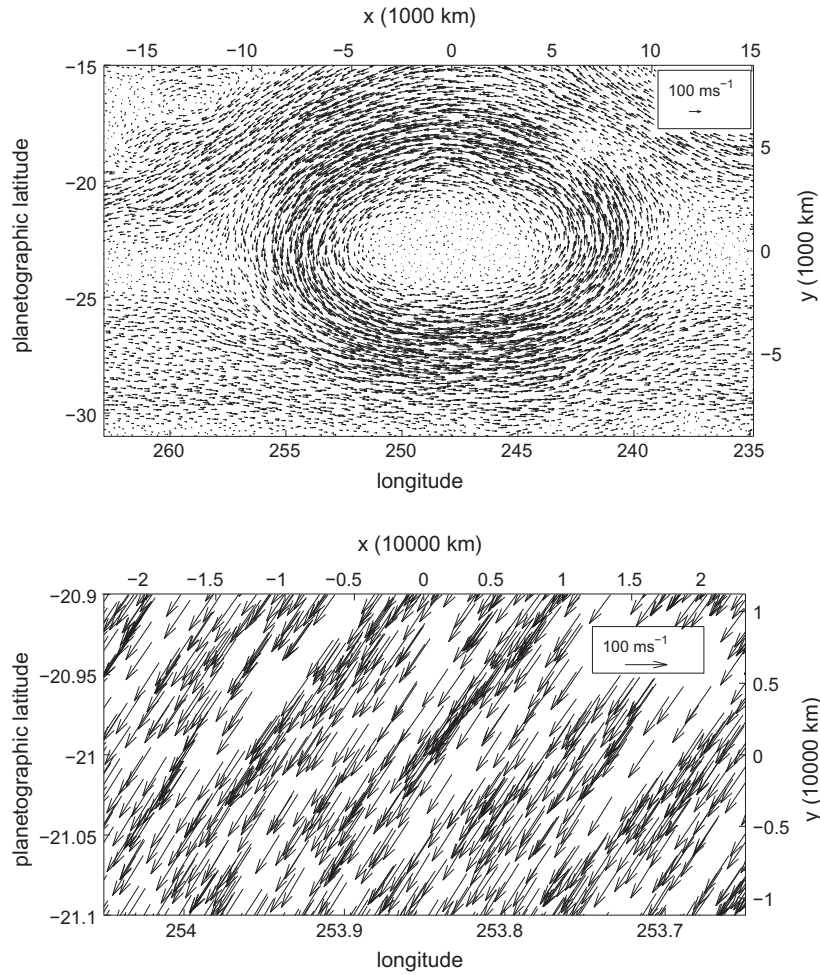


Fig. 1. GRS: velocities extracted from HST 2006 observations with the automated ACCIV method. Top panel: 9124 velocity vectors sampled randomly from the full set of ~ 2.8 million velocity vectors extracted with ACCIV (of which $\sim 140,000$ are independent) (Asay-Davis et al., 2009). We plot only a small sample, containing fewer than 10% of the velocity vectors, because it would be difficult to plot them all. Bottom panel: All of the 940 ACCIV-extracted velocity vectors (of which ~ 50 are independent) within a $0.4^\circ \times 0.2^\circ$ box centered near -21° latitude and 253.85° longitude (i.e., in the northwest part of the high-speed collar in the top panel). Note that the vectors are closely spaced and consistent in direction and magnitude, so interpolating the velocity from the set of vectors can be easily done.

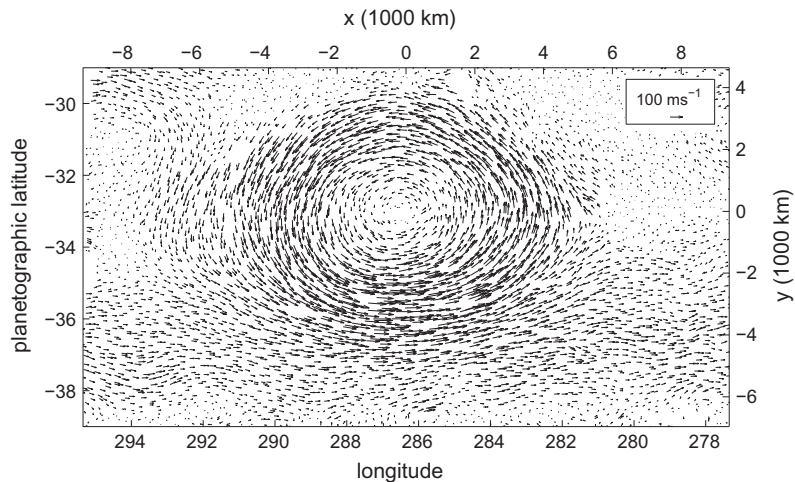


Fig. 2. Oval BA: CIV-extracted velocities from HST 2006 observations. Nine-thousand five-hundred and thirty-seven velocity vectors sampled randomly from the full set of $\sim 140,000$ vectors (of which $\sim 63,000$ are independent) (Asay-Davis et al., 2009). We plot only this small sample, containing fewer than 16% of the total number of independent vectors because it would be difficult to plot them all.

and purely zonal (i.e., velocities point only in the east–west direction). We write this *far-field* flow as $u^\infty(y)\hat{x}$, where x and y are the

local east–west and north–south coordinates, and \hat{x} is the unit vector in the east direction. Far-field velocities were first measured

Table 1

Observed velocity fields and uncertainties that are modeled in this study. All fields were extracted and uncertainties computed with the Advection Corrected Correlation Image Velocimetry (ACCIV) method with the exception of the HST observation of the Oval BA taken on April 2006, which was extracted with Correlation Image Velocimetry (CIV). The definition of *independent vector* is given in Asay-Davis et al. (2009). The *scatter uncertainty* and the *correlation uncertainty* are two separate measures of the uncertainty in the extracted velocities (see Section 2). The entries in the table show the RMS average of the corresponding uncertainty. (In Asay-Davis et al. (2009), the RMS scatter uncertainty is referred to as the 1σ uncertainty.)

Spacecraft	Date	Observed vortex	Number of independent vectors	RMS scatter uncertainty (m s^{-1})	RMS correlation uncertainty (m s^{-1})
Galileo	June 1996	GRS	42,000	1.2	2
Cassini	December 2000	GRS	26,000	4.5	7
HST	April 2006	GRS	140,000	4.5	5
Cassini	December 2000	Oval BA	4200	3.0	6.5
HST	April 2006	Oval BA	63,000	5.5	9.5

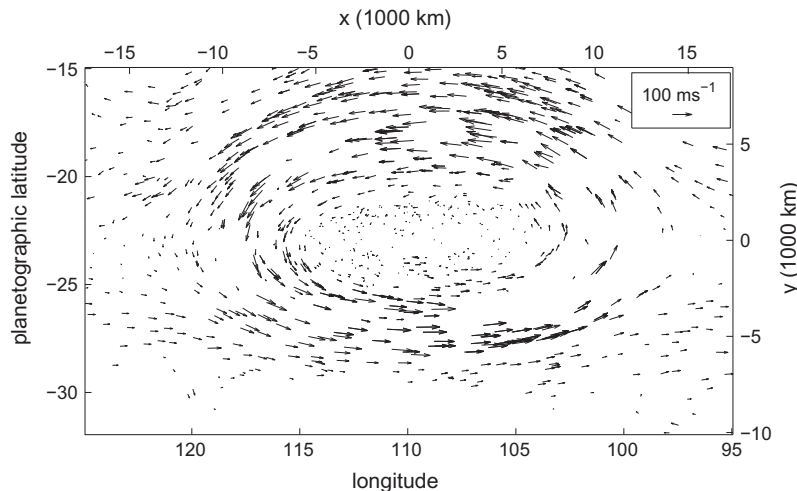


Fig. 3. GRS: velocities extracted from Voyager 2 images with a manual method. All of the 1256 velocity vectors (Beebe, R., personal communication, 1988) that were obtained from Voyager 2 images using a manual extraction method are shown. None of the vectors shown here lie within the $0.4^\circ \times 0.2^\circ$ region shown in the bottom panel of Fig. 1. With this set of vectors there is, on average, one vector per five $0.4^\circ \times 0.2^\circ$ regions, so interpolating the velocity with this set of vectors is difficult.

from observations in 1979 (Limaye, 1986) and have since been measured from many other spacecraft (cf., Simon and Beebe, 1996; Simon, 1999; García-Melendo and Sánchez-Lavega, 2001; Porco et al., 2003). The latitudes where the zonal velocities have their extrema have remained somewhat constant over the last 30 years as have the values of the meridional shears of the zonal velocity at the current mean latitudes of the GRS and Oval BA.² However, the local maxima and minima of the zonal velocities have changed over the last 30 years by $\sim 11 \text{ m s}^{-1}$ (approximately 10% of the maximum zonal velocity). Ideally, our models for each jovian vortex would be computed with images of the vortex coupled with images of the far-field that were taken at the same time. Unfortunately, all of the required images of the far-field zonal flows do not exist. In particular, we do not have an observed zonal flow from 2006. More significantly, using Voyager-approach images, Limaye (1986) showed that the far-field zonal flow has weekly variability of the same order as the decadal variability. Asay-Davis et al. (2010) found even shorter term variability of $\sim 11 \text{ m s}^{-1}$ and concluded that it was not due to observational uncertainty (because the variability was approximately twice as large as the 5 m s^{-1} correlation uncertainty) but was due either to temporal variability over 10 h (a jovian day) or due to variability in the direction or magnitude as a function longitude. These results cast doubts on the assumption of a far-field, steady, purely zonal flow. Nonetheless, to make pro-

gress here, we make this assumption and use the zonal profile derived from Voyager images (Limaye, 1986) in all our models.

3. Equations and physically-based, reduced-parameter model

3.1. Equations

The models used in this paper are steady (or time-independent) solutions of the 2D quasigeostrophic (QG) equations (Pedlosky, 1987), when viewed in a uniformly-translating frame that has east–west speed U with respect to System III. Thus all the vortices computed in this paper have a constant east–west drift speed U with respect to System III. In the following sections, for brevity, a model is sometimes referred to as a steady-state solution, although strictly speaking, a model is steady only in a frame translating with the vortex, and is not steady in System III unless $U = 0$ for that model. The QG equations for the potential vorticity q are:

$$\left(\frac{\partial}{\partial t} + \mathbf{v} \cdot \nabla\right)q = 0, \quad (1)$$

$$q(x, y, t) \equiv \left[\left(\nabla^2 - \frac{1}{L_r^2} \right) \frac{gh}{f_0} \right] + \frac{gh_b(y)}{L_r^2 f_0} + \beta y, \quad (2)$$

$$\mathbf{v} \equiv \hat{\mathbf{z}} \times \nabla \frac{gh}{f_0}, \quad (3)$$

where g is reduced gravity in the weather layer, h is the free-surface height of the upper layer, $h_b(y)$ is the height of the rigid bottom topography, \mathbf{v} is the weather layer's velocity in System III, $\hat{\mathbf{z}}$ is the local vertical unit vector, β is the local gradient of the Coriolis

² The shear was determined by fitting a least-squares straight line to the far-field, zonal velocity from between $23 \pm 3.5^\circ\text{S}$ for the GRS, and $33 \pm 1^\circ\text{S}$ for the Oval BA. The shear, defined to be the negative of the line's slope, is found to be $1.4 \pm 0.1 \times 10^{-5} \text{ s}^{-1}$ for the GRS and $1.2 \pm 0.2 \times 10^{-5} \text{ s}^{-1}$ for the Oval BA.

parameter $f(y)$, f_0 is the local value of $f(y)$, and L_r is the local Rossby deformation radius (Pedlosky, 1987). The only independent dynamical variable in Eqs. (1)–(3) is the free-surface height h ; q and \mathbf{v} are slaved to h through Eqs. (2) and (3).

Previous researchers (Dowling and Ingersoll, 1989; Marcus, 1993; Shetty et al., 2007) parameterized the influence of deep layers on the jovian weather layer with the height $h_b(y)$ of the rigid bottom topography. However, it is more convenient (but equivalent) to use the PV $q^\infty(y)$ of the far-field zonal flow $u^\infty(y)\hat{\mathbf{x}}$. From Eq. (2), there is a one-to-one relation between $h_b(y)$ and $q^\infty(y)$:

$$q^\infty(y) \equiv \left(\frac{d^2}{dy^2} - \frac{1}{L_r^2} \right) \frac{gh^\infty}{f_0} + \frac{gh_b(y)}{f_0 L_r^2} + \beta y, \quad (4)$$

where $h^\infty(y)$ is the free-surface height of the far-field zonal flow, defined by:

$$\frac{1}{f_0} \frac{d(gh^\infty)}{dy} \equiv -u^\infty(y), \quad (5)$$

and where the integral of h^∞ over the computational domain is arbitrarily defined to be zero.³ Because $u^\infty(y)$, β and f_0 are known for the domain of interest, and because the best-fit value of L_r is computed for each of our models, we can use $q^\infty(y)$, rather than $h_b(y)$, in our parameterization. The computational domains for our models of the GRS and the Oval BA are substantially bigger than the vortices themselves. We use a 60° longitude \times 30° latitude computational domain (with 1200×600 Fourier modes) for the GRS, and a 30° longitude \times 30° latitude domain (with 600×600 Fourier modes) for the Oval BA. The domain is sufficiently large to include the jet streams just north and south of the GRS and Oval BA.⁴

3.2. Reduced-parameter model

The fast-solver that computes steady-state (in the frame translating with the vortex) solutions of the QG Eqs. (1)–(3) is an extension of the one we used in Shetty et al. (2007) and is described in more detail in Shetty (2008). The code typically requires 20–30 iterations to converge to a steady-state solution, where each iteration has the same computational expense as a single time step of an initial-value solver of the same equations. Instead of requiring an initial velocity field, the steady-state finder requires that we specify: (1) $u^\infty(y)$; (2) the PV along the north–south line at the extreme right-hand side of the computational domain; and (3) the values of the PV along an east–west line that passes through the vortex. For the GRS, we choose that east–west line to be the latitude 23°S , and for the Oval BA, we choose it to be latitude 33°S . (Based on observations, these latitudes are the principal east–west axes of these two vortices.) The PV along these two lines remains fixed as the steady-state finder is iterated. Because the north–south line is asymptotically far from the vortex, specifying its PV is equivalent to specifying $q^\infty(y)$. To simplify our choices of the PV along these two lines, we exploit the fact that we seek models of the Oval BA or GRS that consist of a compact region of PV embedded in the far-field zonal flow $u^\infty(y)$. Numerical simulations of the QG equations show that the velocities tend to evolve to form

³ A “gage” constant can be added to h^∞ , h_b and/or h , representing a shift in origin or the vertical coordinate. Such a shift has no effect on the velocity or any other observable quantity because h acts as a stream function and only its spatial derivative enters into the dynamics. A change in gage will change the PV by a constant value. We have arbitrarily chosen the gage for h_b such that the PV along the southern boundary of our computational domain is zero.

⁴ The technique of embedding a flow of interest, in this case the GRS or Oval BA, that is a small part of a much larger flow into a spatially-periodic computational domain that is larger than the flow of interest and much smaller than the larger flow is a well-established computational method (cf., Hawley and Balbus, 1992; Spalart, 1998).

flows with compact patches of PV. In these cases the flow is characterized by the curves that mark the boundaries of the patches and the distribution of PV within the vortices. For these reasons, we use the model that was used for the GRS in Shetty et al. (2007) and illustrated in Fig. 4. Here, the GRS or Oval BA is represented by two nested patches of PV: the inner and outer patches have east–west diameters (along the east–west principal axis) of lengths $(D_x)_2$ and $(D_x)_1$, respectively. The PV in the inner patch of the vortex is q_1^{VOR} , and the PV in the annular region between the outer boundary of the inner patch and the boundary of the outer patch is q_2^{VOR} . More patches can be used if necessary, but two patches were found to be sufficient to produce good fits to the observed ACCIV-extracted velocities. Note that the shapes of each patch are not free parameters but are computed by the steady-state finding code. Our original model also included finite widths in the jumps in the PV at the inner and outer boundaries of the patches that make up the Oval BA and GRS. However, best-fit values of those widths turned out to be approximately zero in all of our models, so to simplify the presentation of our results in this paper we treat those jumps as infinitely-thin interfaces.

We specify the value of $q^\infty(y)$ by noting that observations (Read et al., 2006) and numerical experiments (Cho and Polvani, 1996; Marcus et al., 2000) suggest that the far-field PV $q^\infty(y)$ is piecewise constant; that is, the zonal flow is made of regions of nearly uniform PV and interfaces where the PV varies rapidly. Thus in each calculation of a jovian vortex, we require that the far-field PV $q^\infty(y)$ of the zonal flow consist of three pieces of uniform PV. One interface between the patches is south of the vortex center with a jump in PV of ΔQ_E . Asymptotically far from the vortex, the latitude of this interface is y_E . Asymptotically far from the vortex, the other jump is at latitude y_W , north of the vortex center. Its PV jump is ΔQ_W . It will turn out that latitudes y_E and y_W correspond to the approximate latitudes of the peaks of the far-field eastward-going and westward-going jet streams neighboring the vortex. Unlike the interfaces of the PV jumps of the vortices, the interfaces of the zonal flow at y_E and y_W have finite widths of δ_E and δ_W , respectively. Thus q^∞ is discretized as:

$$q^\infty(y) \equiv \frac{\Delta Q_E}{2} \left(\tanh \frac{y - y_E}{\delta_E} + 1 \right) + \frac{\Delta Q_W}{2} \left(\tanh \frac{y - y_W}{\delta_W} + 1 \right). \quad (6)$$

Thus, our model consists of 11 parameters: L_r , $(D_x)_1$, $(D_x)_2$, q_1^{VOR} , q_2^{VOR} , y_E , y_W , ΔQ_W , ΔQ_E , δ_E , and δ_W . Once the 11 parameter values are specified, the fast-solver finds a uniformly translating equilibrium solution to Eqs. (1)–(3) with those values. As mentioned in Shetty et al. (2007), the fast-solver is not sensitive to the choice of initial shapes of the contours, which suggests that the equilibrium contour shapes are uniquely determined by the choice of parameter values. The shapes of the interfaces are computed along with the value of U , the rate at which the vortex drifts eastward with respect to System III. Despite the fact that the model has only 11 free parameters, the best-fit models are good fits to the observations, as shown in the next section. The good fit is due to the facts that (1) the models are true equilibrium solutions to the equations of motion, (2) thousands of sets of parameter values were examined to determine the best fit, and (3) the model is physically motivated.

3.3. Computing best-fit parameters

For each of the five sets of observed, ACCIV-extracted velocities with uncertainties given in Table 1, we searched $\sim 10,000$ sets of parameter values to find the best-fit. The search was carried out using the genetic algorithm (GA) described in Appendix. The set of best-fit parameter values was defined to be the one that minimized a cost-function $(C_{\text{vel}} + C_{\text{area}})/2$. The component C_{vel} of the cost-function measures the difference between the model velocity

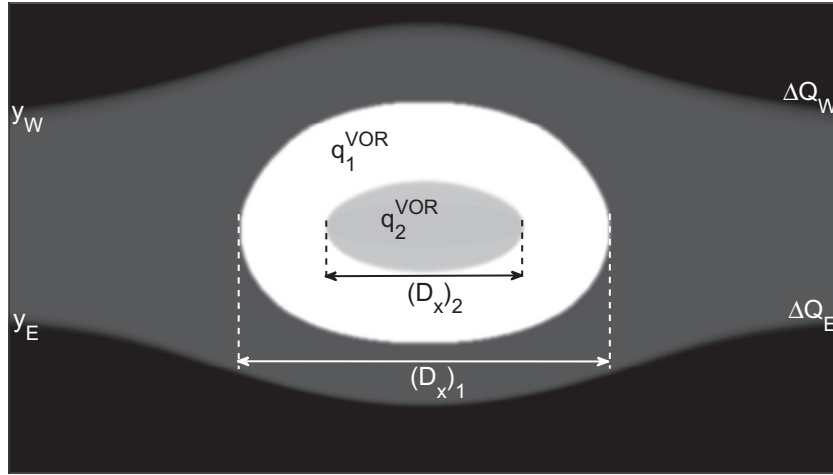


Fig. 4. Schematic of the PV of the reduced model of a jovian vortex illustrating its input parameters. In our reduced model of the GRS, the PV of the vortex is compact and consists of two nested patches of uniform PV with values q_2^{VOR} and q_1^{VOR} as shown. Different values of PV are indicated by different shades of gray. The outer boundaries of these patches have infinitesimal widths, and the diameters of the east–west principal axes of the inner and outer patches are $(D_x)_2$ and $(D_x)_1$, respectively. In our models, the GRS and Oval BA are each embedded in a zonal flow that consists of three uniform patches of PV. Far from the vortex, the zonal flow is exactly parallel to the east–west axis, and the latitudes of the two boundaries between these three patches asymptote to y_E and y_W . At these two boundaries the “jumps” or changes in the values of the PV are ΔQ_E and ΔQ_W , respectively. These boundaries have widths of δ_E and δ_W . The GRS or Oval BA, represented by the compact, nested patches of PV, deform the contours of the boundaries between the patches of zonal PV so that they bend around the vortex. In our model, the locus of the four contours between the five patches of uniform PV are all computed numerically and determined such that the flow (which is uniquely determined by the PV) is a steady solution to the QG equations of motion in a frame translating eastward with velocity U (where U is uniquely determined by the equations of motion).

$\mathbf{v}^{\text{mod}}(\mathbf{x})$ found by the fast-solver and the observed velocity $\mathbf{v}^{\text{obs}}(\mathbf{x})$. To sample the flow field uniformly, we compute the difference over N ($\sim 10^3$) computational grid points $\mathbf{x}(i)$, and we weight the difference at each grid point with the value of the *scatter uncertainty* $\delta \mathbf{v}^{\text{obs}}(i)$ of the ACCIV-extracted velocity at that grid point:

$$C_{\text{vel}} \equiv \frac{1}{2N} \sum_{i=1}^N \frac{|\mathbf{v}_x^{\text{mod}}(\mathbf{x}_i) - \mathbf{v}_x^{\text{obs}}(\mathbf{x}_i)|}{\delta v_x^{\text{obs}}(\mathbf{x}_i)} + \frac{|\mathbf{v}_y^{\text{mod}}(\mathbf{x}_i) - \mathbf{v}_y^{\text{obs}}(\mathbf{x}_i)|}{\delta v_y^{\text{obs}}(\mathbf{x}_i)}. \quad (7)$$

We use an L_1 -norm in the definition of C_{vel} because it is less sensitive to outliers in the observations (cf., Press et al., 1988), although we obtained similar results with an L_2 -norm. The computational grid points used in the definition of C_{vel} lie within an oval shaped region surrounding the vortex as shown in Figs. 22 and 23. Points outside this region are not included in C_{vel} because they are sufficiently far from the PV anomaly of the vortex that their velocities are insensitive to the model parameters. Note that the locations of the ACCIV-extracted velocities and the corresponding *scatter uncertainties* do not necessarily coincide with the locations of computational grid points and must therefore be interpolated at the computational grid points to compute the cost-function. However, because the is suggestive of extracted velocities is much smaller than the computational grid resolution (see Figs. 1–3), the errors introduced by interpolation are much smaller than the *scatter uncertainties*. The procedure for interpolating the velocities and *scatter uncertainties* to the computational grid is described in Appendix. Typically, a value of $C_{\text{vel}} \sim 1$ distance between a good fit to the observations. Here however, the *scatter uncertainties* used in the definition of C_{vel} underestimate the actual uncertainties by a factor of two as described in Section 2.1, and so a value of $C_{\text{vel}} \sim 2$ is more representative of a good fit to the observations.

The second component of the cost-function is $C_{\text{area}} \equiv |A^{\text{mod}} - A^{\text{obs}}| / \delta A^{\text{obs}}$, where A^{mod} is the area of the PV anomaly of the vortex computed with the steady-state finder, A^{obs} is the area of the anomaly from observations, and δA^{obs} is the uncertainty in A^{obs} . (See Tables 2 and 3 for how we compute A^{mod} . See Section 5.2 for how we compute A^{obs} and its uncertainty δA^{obs} .) There was little difference between the set of best-fit parameters found with $(C_{\text{vel}} + C_{\text{area}})/2$ and those found when C_{area} was excluded from the cost-function definition. However, the genetic algorithm that used

Table 2

The best-fit parameters for the GRS. Values are obtained with a genetic algorithm. Uncertainties are computed using the Monte Carlo boot-strap method in Section 3.4. The best-fit parameters for the Voyager 1 velocity field are obtained from the trait-matching algorithm used in Shetty et al. (2007), and their uncertainties were not computed. Quantities below the double horizontal lines are not parameters of our model, but rather, quantities derived from it. The RMS error listed in the table is the RMS value of the unweighted difference between the velocity of the best-fit model and of the observed velocity field within the oval shaped domain shown in Fig. 22. The RMS errors are small compared to the characteristic flow velocities and the best-fit models reproduce large-scale features of the flow as shown in Figs. 5–7. Although the RMS errors for all three datasets are similar, the value of C_{vel} for the Galileo dataset is large because the uncertainties in the Galileo velocities are small owing to the small effective resolution of the Galileo images (see Section 4.1 for details). Areas in the Table are from the best-fit models and are defined to be the areas A^{mod} enclosed by the model’s outer contour of the PV, i.e., the contour with east–west diameter $(D_x)_1$. The aspect ratio is defined as the ratio of the east–west diameter $(D_x)_1$ to north–south diameter of the outer contour of PV for the vortex.

Parameter	Unit	Voyager 1 (1979)	Galileo (1996)	Cassini (2000)	HST (2006)
$(D_x)_1$	km	19,500	18,100 ± 170	16,400 ± 240	15,400 ± 100
$(D_x)_2$	km	12,000	10,400 ± 850	9000 ± 990	8300 ± 530
L_r	km	2400	2210 ± 120	2320 ± 160	2300 ± 70
q_1^{VOR}	10^{-5} s^{-1}	10.5	12.3 ± 2.1	12.4 ± 2.1	12.0 ± 0.7
q_2^{VOR}	10^{-5} s^{-1}	6.0	9.2 ± 1.3	8.5 ± 1.4	7.5 ± 0.5
ΔQ_E	10^{-5} s^{-1}	1.9	4.1 ± 2.2	4.0 ± 0.7	3.4 ± 1.0
ΔQ_W	10^{-5} s^{-1}	−5.6	−5.9 ± 2.5	−6.3 ± 1.2	−7.0 ± 0.9
y_E	°S	26.0	25.9 ± 0.4	26.1 ± 0.4	25.6 ± 0.3
y_W	°S	20.0	19.9 ± 0.5	20.1 ± 0.3	19.9 ± 0.3
δ_E	km	300	200 ± 200	200 ± 200	400 ± 200
δ_W	km	1000	800 ± 200	700 ± 200	700 ± 200
C_{area}	–	–	0.1	0.1	0.1
C_{vel}	–	–	16.0	5.8	3.8
RMS error	m s^{-1}	–	15	16	14
Area	10^6 km^2	142.3	146.7 ± 0.2	136.8 ± 0.8	120.9 ± 0.5
Aspect ratio	–	2.2	1.9 ± 0.1	1.6 ± 0.1	1.6 ± 0.1

both components required fewer trials to converge to the best-fit parameter values.

3.4. Computing uncertainties in best-fit parameters

One approach to deriving the uncertainties in the best-fit parameters is to artificially perturb the observed velocity field

Table 3

Best-fit values of the parameters of our models of the Oval BA listed as in Table 2. The large value of C_{vel} for the Cassini data is due to the fact that the model is a poor fit to the observations at the northern boundary of the Oval, where the observed streamlines of the velocity are pulled north into a cusp (Asay-Davis et al., 2009). We believe this unusual behavior along with the large value of C_{vel} indicate that the Oval BA was not in a steady or uniformly-translating state in December 2000.

Parameter	Unit	Cassini (2000)	HST (2006)
$(D_x)_1$	km	7080 ± 140	7100 ± 90
L_r	km	1860 ± 230	1900 ± 150
q_1^{VOR}	10^{-5} s^{-1}	14.2 ± 1.9	13.3 ± 1.3
ΔQ_E	10^{-5} s^{-1}	1.8 ± 1.3	1.4 ± 0.5
y_E	$^\circ\text{S}$	35.0 ± 1.1	35.3 ± 0.7
δ_E	km	400 ± 100	400 ± 200
C_{area}	–	0.1	0.1
C_{vel}	–	11.0	4.0
RMS error	m s^{-1}	14	9
Area	10^6 km^2	32.1 ± 0.4	30.8 ± 0.2
Aspect ratio	–	1.2 ± 0.1	1.2 ± 0.1

using the distribution of uncertainty at each measurement point, and then determine how those perturbations propagate into the best-fit parameter values. For the observed velocity fields used in this paper, the distribution of the uncertainty at each measurement point is not known. We therefore compute uncertainties using a boot-strap Monte Carlo method (Press et al., 1988) because a boot-strap method does not require the distribution. In this method an ensemble of new observed velocity fields is generated, not by perturbing the velocity field, but rather by uniformly sampling the original set of velocity vectors. Each sample velocity field in the ensemble is a random subset of the original field's velocity vectors. A corresponding ensemble of best-fit models of the sampled fields is computed. The uncertainty in the value of a best-fit parameter, such as the deformation radius, is defined to be the standard deviation of the best-fit values of the deformation radius found from the ensemble of best-fit models. For the results in this paper, an ensemble consisting of 10 velocity fields was used to estimate uncertainties. Adding more velocity fields to the ensemble did not have a significant effect on the estimated uncertainties.

4. Results: best-fit solutions and comparison with observations

4.1. GRS

Table 2 shows the best-fit parameters for the GRS and the corresponding values of C_{vel} , C_{area} and the value of the RMS difference between the best-fit model velocity field and the observed velocity field. The best-fit models have $C_{vel} = 16.0$, $C_{vel} = 5.8$ and $C_{vel} = 3.8$ for the Galileo, Cassini and HST datasets respectively. Although the value of C_{vel} for the Galileo best-fit model is approximately 3 times larger than the value of C_{vel} for the Cassini or HST best-fit models, the quality of fit for all three models is similar. This is because the uncertainties with which C_{vel} is weighted are approximately three times smaller for the Galileo data than for the Cassini or HST data. The smaller uncertainty for the Galileo data is reflective of the fact that the Galileo images have smaller effective resolution than either the Cassini or HST images (Asay-Davis et al., 2009). Furthermore, the (unweighted) RMS difference between the observed and best-fit velocities for the Cassini, Galileo and HST datasets are all approximately 15 m s^{-1} despite the fact that these datasets have very different uncertainties, effective resolutions, and numbers of independent vectors.

The values of C_{vel} for the best-fit models are larger than the value of $C_{vel} \sim 2$ that would be suggestive of a good fit. However,

most of the contribution to C_{vel} occurs outside the vortex where the flow is known to contain small-scale time-dependent turbulent features that cannot be accounted for by the 1.5-layer QG equations (we return to this point again in Section 7 when we discuss limitations of the model). Similarly, although the 15 m s^{-1} RMS error for the best-fit models is approximately 2–3 times larger than the RMS uncertainties listed in Table 1, the RMS error is much smaller than the characteristic velocities for these datasets and the best-fit models do a good job of reproducing large-scale features of the flow. This is best illustrated by plots of the velocity along the east–west and north–south principal axes in Figs. 5–7, which show that the best-fit models reproduce the velocity profile of the GRS's high-speed circumferential jet and quiescent core. We note that the figures show larger discrepancies at the locations of the peak velocities, where the model systematically predicts larger velocities than are observed. However, these discrepancies can be attributed to the fact that all methods of extracting velocities from tie-point pairs, regardless of whether they are from automated or manual methods, tend to systematically underestimate or “round” the observed velocity peaks (Asay-Davis et al., 2009). The agreement between the model and observed velocities at other locations inside the GRS is similar to the agreement along the principal axes, and the errors are consistent with the RMS error given in Table 2. In addition, all best-fit models have $C_{area} < 1$ implying that they capture the observed vortex area to within the observational uncertainty.

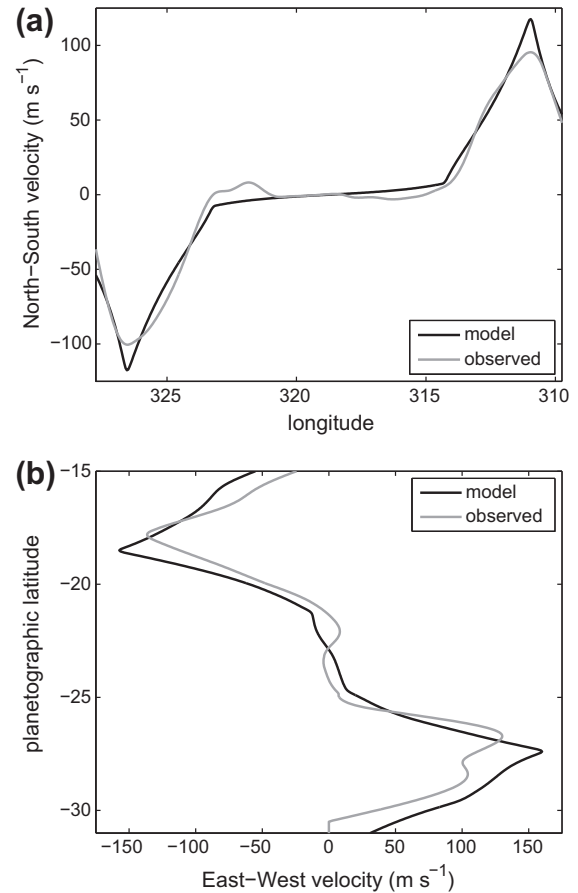


Fig. 5. GRS: comparison of observed (Galileo, June 1996) velocities with model velocities computed with the best-fit parameter values. Gray curves are the model velocities and black curves are observed velocities. (a) North–south velocities along the east–west principal axis of the GRS. (b) East–west velocities along the north–south principal axis of the GRS.

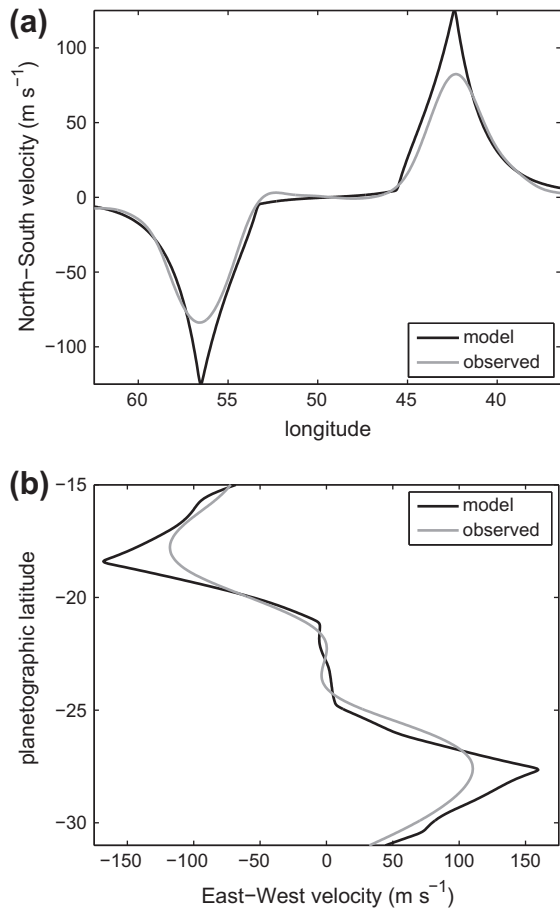


Fig. 6. GRS: comparison of observed (Cassini, December 2000) velocities with model velocities computed with best-fit parameter values. Shown as in Fig. 5.

4.2. Oval BA

Table 3 shows the best-fit parameters for the Oval BA and corresponding values for C_{vel} and C_{area} . Fig. 8 compares the observed and best-fit velocities along the principal axes of the Oval BA for the HST data from 2006. With the exception of the western wake of the Oval, the fit is good, and this is quantitatively confirmed by the low cost-function $C_{vel} = 4.0$ and low RMS error of 9 m s^{-1} .

The best-fit model to the Oval BA from Cassini data has a large cost-function value of $C_{vel} = 11.0$ and a large RMS error of 14 m s^{-1} . The images used in this fit were taken in December 2000, and Fig. 9(b) shows that the observed locations of the peak east-west velocities along the north-south principal axis (which are near the northern- and southern-most extremities of the PV anomaly of the Oval BA), especially in the north, do not coincide with the model's locations of the peaks. The velocities extracted from the Cassini images of the northern boundary of the Oval BA show a prominent cusp-like feature (see Fig. 25b and e and description in Asay-Davis et al. (2009)), which is atypical of a *steady* or *uniformly-translating* vortex. This cusp, along with the inability to match the velocity to a steady-state solution to the equations of motion, suggest that in December 2000 the Oval BA was in a transient state. Transients in the Oval BA at that time are plausible because the Oval BA was formed by the merger of Oval FA and Oval BE in March and April 2000, so the Cassini images were taken only 8 months or ~ 50 vortex-turn-around times of the Oval after it formed. Numerical simulations in 2D of merging vortices of equal PV strengths and equal areas that are embedded in a shearing zonal flow show that it takes approximately 50–100 vortex-turn-

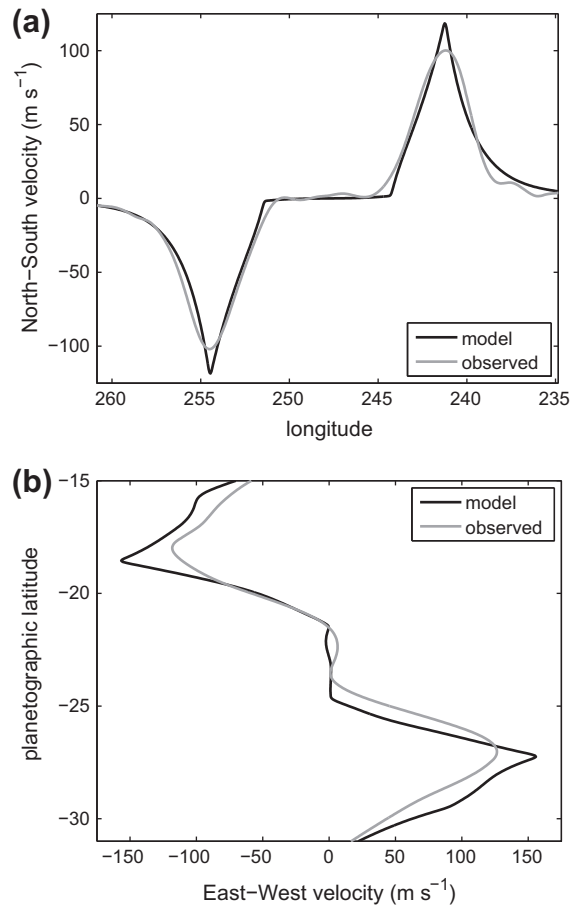


Fig. 7. GRS: comparison of observed (HST, April 2006) velocities with model velocities computed with best-fit parameter values. Shown as in Fig. 5.

around times for a vortex to come to a steady equilibrium after it is formed by merger (Marcus, 1993). Therefore, the velocity fields on the northern side of Oval BA are particularly suspect, and any quantity that is derived from them should be viewed with caution, especially when looking for temporal changes in the Oval BA or finding explanations for why it changed its color from white to red in late 2005.

5. Physical results for the GRS

5.1. Changes in time

Table 2 shows that the east-west diameter $(D_x)_1$ of the GRS's PV anomaly has decreased from $18,100 \pm 170 \text{ km}$ to $15,400 \pm 100 \text{ km}$, or 15% from 1996 to 2006. No other best-fit parameter (except for the east-west diameter $(D_x)_2$ of the core) has changed more than the parameter's uncertainties. Some quantities derived from $(D_x)_1$ also changed more than their uncertainties: the aspect ratio became rounder, decreasing from 1.9 in 1996 to 1.6 in 2006, and during the same time interval, the area of the GRS's PV anomaly decreased by about 18%.

Table 2 shows that the best-fit values of y_E and y_W of far-field jumps in PV occur near the latitudes of the maxima in the far-field jet streams. The jump ΔQ_W in PV in the westward-going jet stream is larger in magnitude than the jump ΔQ_E in the eastward-going jet stream. These two PV jumps have opposite sign, which is consistent with the results found in Shetty et al. (2007) for Voyager 1 data. However the result is surprising, because it confirms that the far-field PV of Jupiter's zonal flow does not decrease *monoton-*

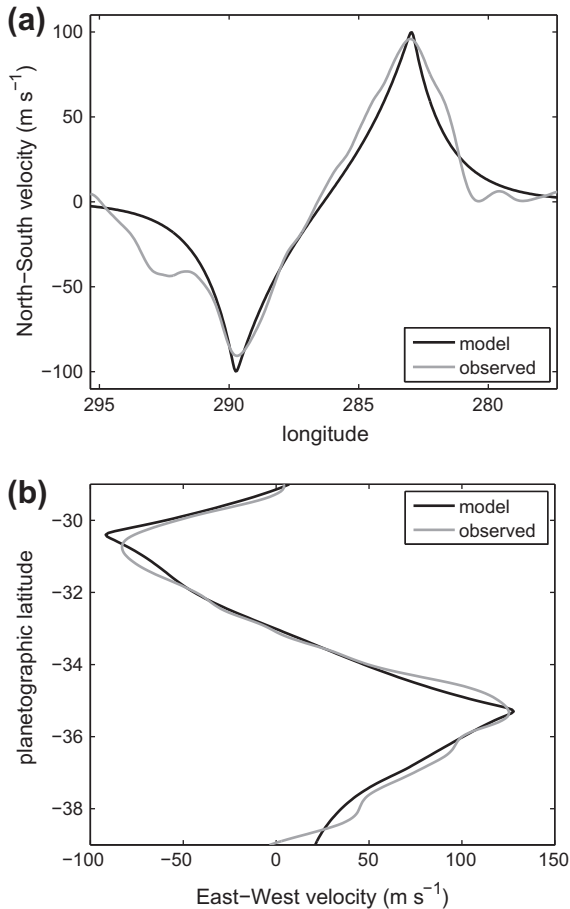


Fig. 8. Oval BA: comparison of observed (HST, April 2006) velocities with model velocities computed with best-fit parameter values. Shown as in Fig. 5.

ically from north to south, contrary to expectations (Marcus, 1993). The physical implications of this result on the GRS are explored below.

5.1.1. Explanations for the decrease in aspect ratio of the PV anomaly of the GRS

For a vortex with uniform PV that is a steady solution to the QG equations and that is embedded in a shearing zonal flow with a uniform PV, the aspect ratio (east-west diameter divided by north-south diameter) of the vortex is a function of only two dimensionless parameters: (1) the ratio of the average shear in the zonal flow to the PV in the vortex and (2) the ratio of the deformation radius L_r to the square root of the area of the PV anomaly of the vortex. If the shear of the zonal flow, deformation radius, and PV of the vortex are held fixed, while the area of the vortex decreases, then the aspect ratio decreases, and the vortex becomes rounder. The physical reason that the aspect ratio decreases is the following. The zonal shear tends to elongate the vortex in the east-west direction. A vortex with large PV compared to the zonal shear acts as if the shear is not present or insignificant and is therefore nearly round. In a QG vortex, the velocity created by a PV element falls exponentially with the distance from the center of the element with an e-folding length of L_r . Thus, if the average radius of a vortex decreases, and the magnitude of the shear of the ambient zonal flow remains fixed, then the vortex becomes rounder. Numerical simulations by Van Buskirk (1991) show that a decrease in the area of the PV anomaly of a vortex usually makes the vortex rounder even in cases where the PV of the vortex or the zonal flow

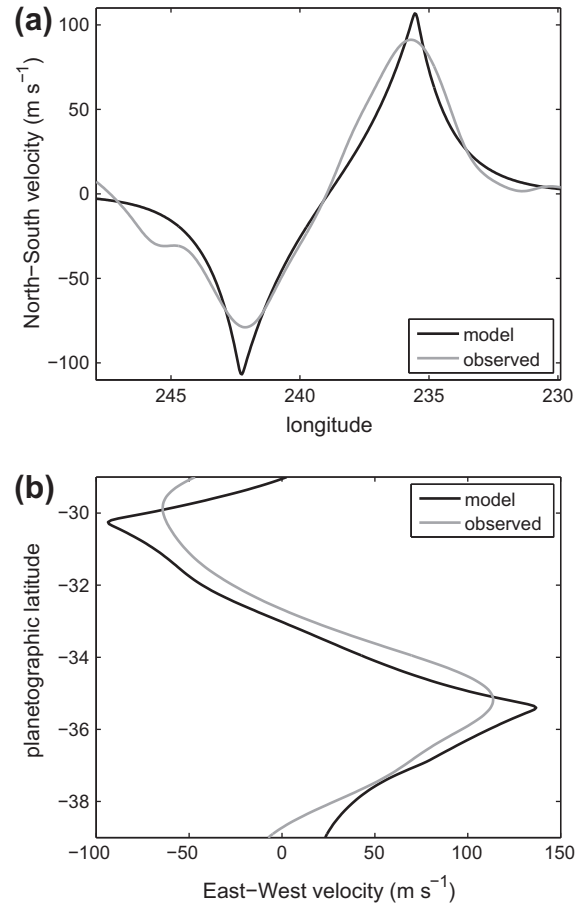


Fig. 9. Oval BA: comparison of observed (Cassini, December 2000) velocities with model velocities computed with best-fit parameter values. Shown as in Fig. 5.

are not uniform and also in cases where the zonal shear is not uniform. This last statement is true for the GRS. That is, the GRS becomes rounder when the area of the GRS is decreased and all other parameters are held fixed. Specifically, if all the parameters in the 11-parameter model of the GRS except for the principal diameters $(D_x)_1$ and $(D_x)_2$ are held fixed at their best-fit values from 1979, and the value of $(D_x)_1$ is then decreased from its best-fit value from the 1979 observations (and the ratio $(D_x)_2/(D_x)_1$ is held fixed) to its best-fit value in 2006, then the area of the GRS monotonically decreases, and it becomes rounder. Thus a rounder GRS is consistent with a decrease in area with no changes in the magnitudes of its PV, in L_r , or in the far-field zonal flow.

5.2. Clouds, maximum velocities, stagnation points, and the location of the PV anomaly

Fig. 10 shows streamlines of the best-fit flow in a frame translating so that the GRS is steady. The heavy closed streamline is the outer boundary of the PV anomaly computed with the best-fit steady solution in Table 2. Superposed with the streamlines is one of the HST images of the GRS clouds from which the velocities used in obtaining the best-fit were extracted. The area of the GRS's cloud cover is significantly greater than the area of the GRS's PV anomaly. Fig. 11 shows two stagnation points where streamlines cross near the GRS. One is directly north of the center of the GRS at latitude 12.5°S , and the other directly south at latitude 32.5°S . Fig. 10 shows that southwest of the northern stagnation point there is a cloud filament aligned with the streamline leading from the stagnation point. Just east of the stagnation point, clouds

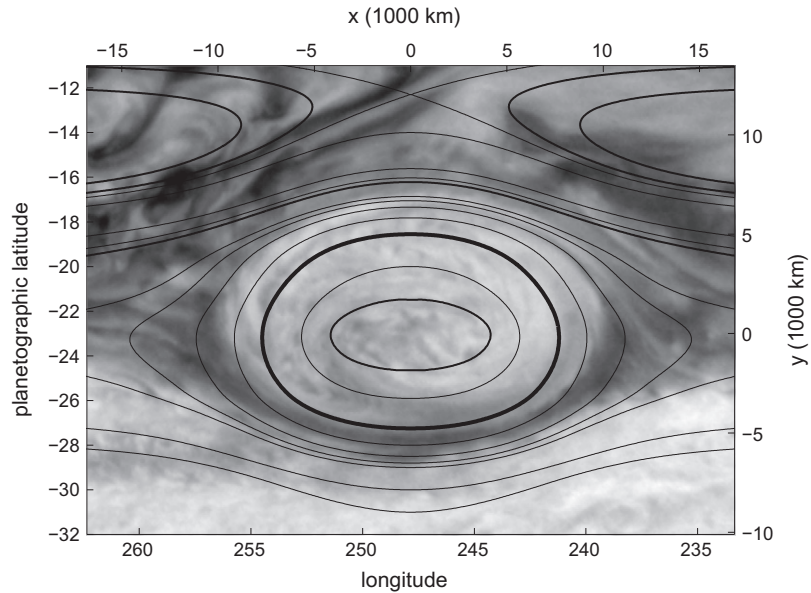


Fig. 10. Clouds and PV of the GRS. Image from HST (April 2006) of the GRS showing its cloud cover. Superposed are the streamlines of the best-fit velocity field. The thick, black closed streamline (third contour out from the center of the GRS) is the outer contour of the PV anomaly of the GRS as computed with the best-fit model. The cloud cover is larger (especially on the northern side) than the PV anomaly. The dark band in the cloud cover (which is bright in the IR) and which marks the southern-most extent of the cloud cover of the GRS is *not* coincident with any part of the contour that marks the outermost boundary of the PV anomaly, and, in fact, is not coincident with any streamline.

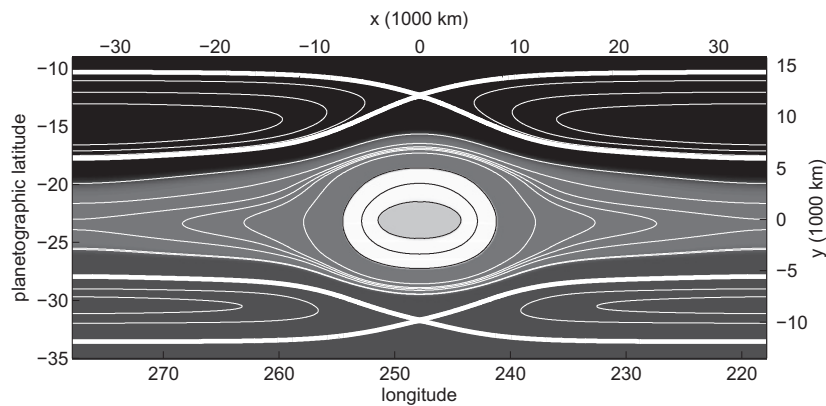


Fig. 11. Stagnation points and PV of the GRS. Streamlines for best-fit model of GRS using HST observations from April 2006, where the stagnation points north and south of the GRS are due to the crossing streamlines indicated with thick, white lines. The value of the PV in the model is indicated with a gray-scale (and consists of five patches). The stagnation points are far from the PV anomaly of the GRS. In contrast, the Oval BA has a stagnation point close to its PV anomaly (see Fig. 19).

appear to be filamenting from the GRS. However, the PV anomaly of the GRS is never closer than 7000 km to the stagnation point, so it would require an enormous temporal fluctuation to allow the stagnation point to interact with the PV and cause it to filament away from the GRS. For this reason, it is highly unlikely that filamentation from the stagnation point could be responsible for the observed decrease in the area of the PV anomaly of the GRS from 1979 to 2006.

The closed curve in Fig. 12 shows the boundary of the model PV anomaly of the GRS as in Fig. 10, but here it is superposed with a broken closed curve that corresponds to contour along which the observed velocity of the GRS has a local maximum. That broken contour was computed by drawing a set of radial “spokes” outward from the center of the GRS and then finding the location of the peak velocity amplitude along each spoke. The broken curve in Fig. 12 is the locus of all of the maxima. The locus of the velocity maxima and the outer boundary of the PV anomaly are nearly the same; however, the locus of the velocity maxima is much more jagged due, in part, to the fact that the observed velocity field shows the

effects of small-scale temporal fluctuations, whereas the PV boundary is the result of a steady-state calculation. The procedure of finding local maxima along spokes amplifies noise in the data, and this also contributes to the jaggedness of the contour. We define the area enclosed by the broken closed curve to be the observed area A^{obs} of the GRS used in determining the cost-function C_{area} . The uncertainty in the observed area δA^{obs} is computed by assuming that the position of the broken curve at each location is uncertain by the effective resolution of the image. The lengths of the east–west and north–south principal axes of the outer PV boundary of the GRS and of the broken contour in Fig. 10 are given in Table 2 and in Asay-Davis et al. (2009), respectively; and they agree to within the uncertainties of $(D_x)_1$ listed in Table 2.

5.3. Ingredients of the GRS

One way to illustrate the physics that governs the GRS is to determine the effects on the GRS of the different PV jumps. For example, the most striking differences between the GRS and the

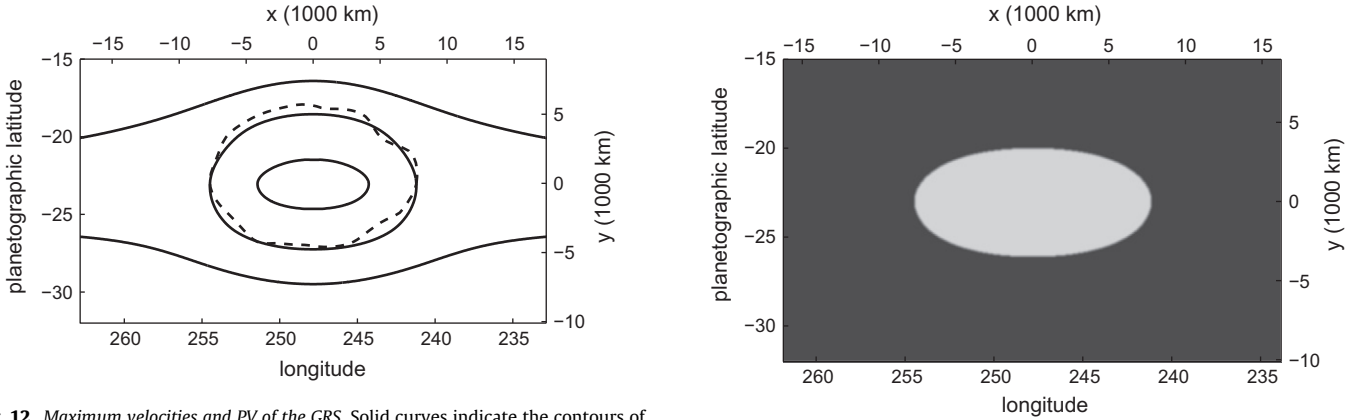


Fig. 12. Maximum velocities and PV of the GRS. Solid curves indicate the contours of the four PV jumps in the best-fit model of the GRS using the HST observations from April 2006. The outermost, closed, solid curve around the GRS indicates the outer boundary of the PV anomaly of the GRS. That boundary nearly coincides with the broken curve, which is the locus of the local maximum velocity of the GRS (see Section 5.2 for details).

other long-lived jovian vortices, such as the Oval BA, is that the GRS is “hollow”: its center is a local minimum, rather than a maximum, of the absolute value of the PV (i.e., $q_2^{VOR} < q_1^{VOR}$). It is this hollowness that makes the velocities in the core relatively small compared with the core velocities of other vortices (cf., compare Figs. 5a and 8a). As Table 2 shows, the GRS has remained hollow from 1979 to 2006. Most hollow vortices are unstable. They rapidly turn themselves “inside out”, and then relax to a new equilibrium that is not hollow (Marcus, 1993). If we constrain our steady-state model of the GRS (using the HST observations from 1996) to have only one PV jump, (i.e., with $q_2^{VOR} \equiv q_1^{VOR} \neq 0$ and $\Delta Q_W \equiv \Delta Q_E \equiv 0$), then we can obtain a steady solution to the QG equations that best-fits the observations subject to the constraints of this restricted model. That solution is shown in Fig. 13. This model accurately captures the locations and magnitudes of the peak velocities along the principal east–west axis, and the correct rate of the velocity fall-off outside the GRS (i.e., in the range $|x| > (D_x)_1/2$) along the east–west axis. This result is consistent with the results of trait-matching (Shetty et al., 2007), which showed that the only ingredients needed for an equilibrium model to correctly reproduce the velocity fall-off rate along the east–west axis is the correct value of L_r . (This result is also consistent with analytic solutions of compact vortices with uniform PV, and $\mathbf{v}^\infty = \mathbf{q}^\infty = 0$. The azimuthal velocity exterior to these vortices decays exponentially with an e-folding length equal to L_r , Marcus, 1993.) Trait-matching showed that, other than L_r , the only ingredients needed to match the locations and magnitudes of the velocity peaks along the east–west axis are properly-tuned values of q_1^{VOR} and $(D_x)_1$. However, because $q_2^{VOR} \equiv q_1^{VOR}$ the constrained-best-fit model in Fig. 13 cannot be hollow, and so it fails to capture the quiet core of the GRS as the unconstrained-best-fit model in Fig. 7 does. In addition, the observed and model velocities disagree along most of the north–south axis. If we loosen our constraints and compute the best-fit model with two PV jumps for the GRS (i.e., with q_2^{VOR} , q_1^{VOR} , $(D_x)_1$ and $(D_x)_2$ as free parameters), but with no PV jumps in the far-field (i.e., with $\Delta Q_W \equiv \Delta Q_E \equiv 0$), then the best-fit model with these restrictions (Fig. 14) is hollow and captures the observed flow all along the east–west principal axis. This model still fails to capture the flow along the north–south axis. As Fig. 15 shows, to capture the observed velocity in the southern part of the GRS along its north–south principal axis, it is sufficient to have a best-fit model with two PV jumps for the GRS (as in Fig. 14) and one jump for the far-field flow (i.e., with ΔQ_E , y_E and δ_E as free parameters). Figs. 7 and 11 show that to capture the observed flow along the entire north–south axis (and, it turns out, over the entire do-

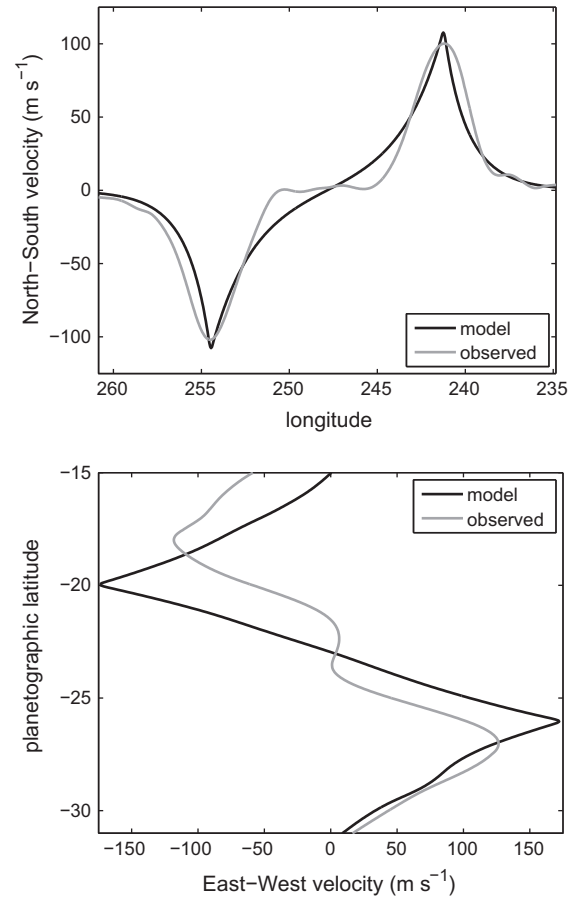


Fig. 13. Constrained best-fit model of the GRS. Here, the model’s PV is constrained to have no jumps in the zonal flow and only one jump for the GRS itself (i.e., $\Delta Q_E \equiv \Delta Q_W \equiv 0$ and $q_2^{VOR} \equiv q_1^{VOR}$). Top panel: PV of the constrained-best-fit model. Middle panel: comparison of the north–south velocities of the model and observations on the east–west principal axis. Bottom panel: Comparison of the east–west velocities along the principal north–south axis. The observations and model are for the HST images of April 2006. Although this constrained model captures the locations and magnitudes of the north–south velocity peaks (middle panel), it fails to make a hollow vortex and does not reproduce the east–west velocity well.

main), four PV jumps are needed, including the one characterized by ΔQ_W , y_W and δ_W . The best-fit models do an excellent job at finding the locations of the velocity peaks along the north–south axis, but, as noted above, the magnitudes of the observed velocity peaks are probably too low due the inherent “rounding” in the velocity extraction methods.

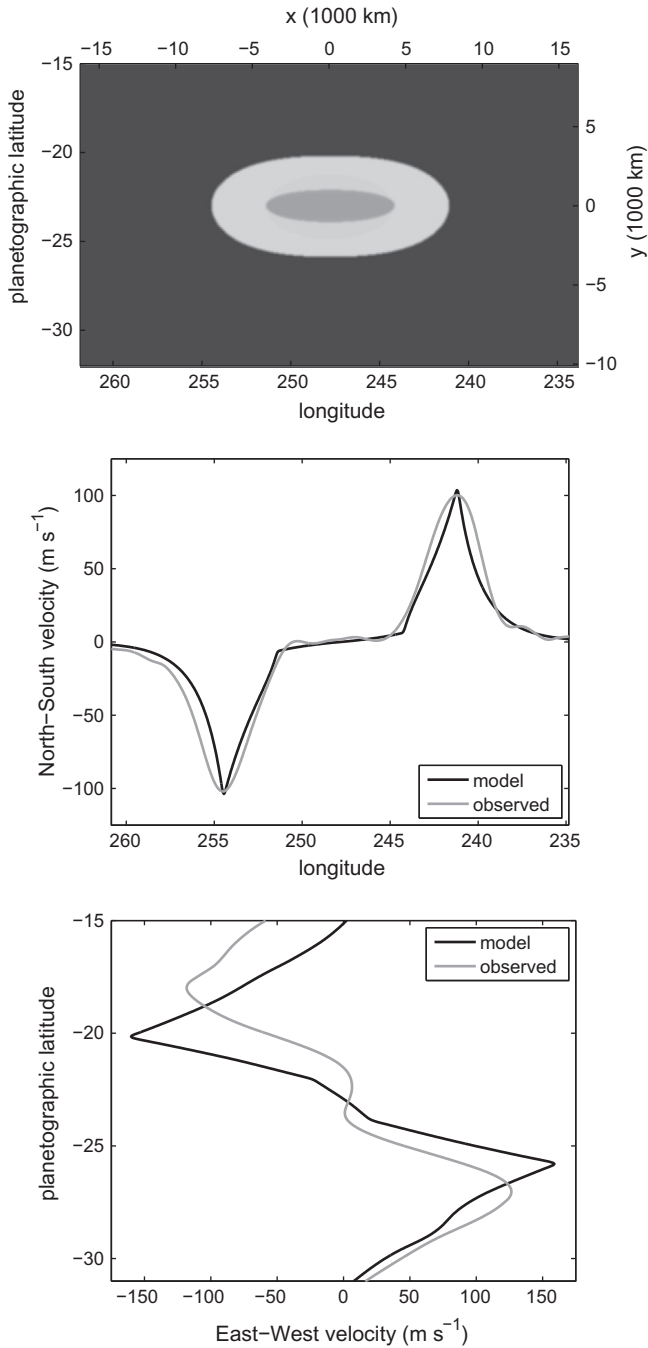


Fig. 14. Constrained best-fit model of the GRS. As in Fig. 13, but here, the model's PV is constrained to have no jumps in the zonal flow and two jumps in the GRS itself (i.e., $\Delta Q_E \equiv \Delta Q_W \equiv 0$). The inclusion of a second PV jump in the model captures the hollowness of the vortex (as well as locations and magnitudes of the north-south velocity peaks). However, the model does not reproduce the east-west velocity well.

5.4. Vortex-zonal flow interaction

To understand the interactions between vortices and zonal flows, it is first necessary to understand that the total PV of the flow is not a linear superposition of the far-field zonal PV and the PV anomaly of a vortex. For example, the total PV of our best-fit GRS model q is shown in the top panel of Fig. 16, and it is not the sum of the best-fit PV q^∞ of the far-field zonal flow (second from top panel in Fig. 16) as defined in Eq. (4) and the best-fit PV anomaly q^{GRS} of the GRS (bottom panel in Fig. 16), which is due

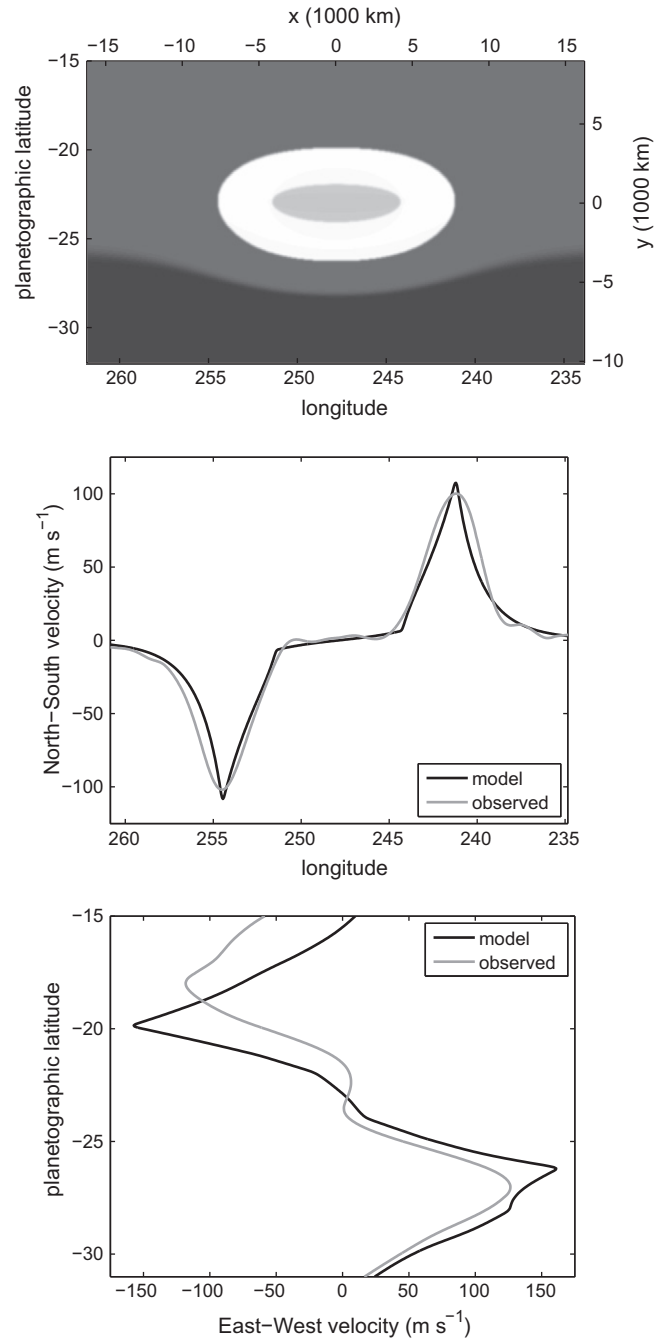


Fig. 15. Constrained best-fit model of the GRS. As in Fig. 13, but here, the model's PV is constrained to have one jump in the zonal flow (south of the GRS) and two jumps in the GRS itself (i.e., $\Delta Q_W \equiv 0$). The inclusion of a PV jump in the zonal flow south of the GRS allows the model to capture the correct location of the eastward-going velocity peak south of the GRS (as well as locations and magnitudes of the north-south velocity and the hollowness of the vortex). However, the model does not reproduce the location of the westward-going velocity peak north of the GRS. One reason that there is only fair agreement between the observed and model values of the magnitude of the eastward-going velocity peak south of the GRS is that the observed velocity peaks are "rounded" by velocity extraction methods (Asay-Davis et al., 2009).

to q_2^{VOR} and q_1^{VOR} . To understand the nonlinearity mathematically, define the interaction PV $q^{INT}(x,y)$ as

$$q^{INT}(x,y) \equiv q(x,y) - [q^\infty(y) + q^{GRS}(x,y)]. \quad (8)$$

Note that $q^{INT}(x,y)$ is not directly defined by the 11 input parameter values of the model, but it is indirectly a function of all of them. The interaction PV is found by numerically computing the

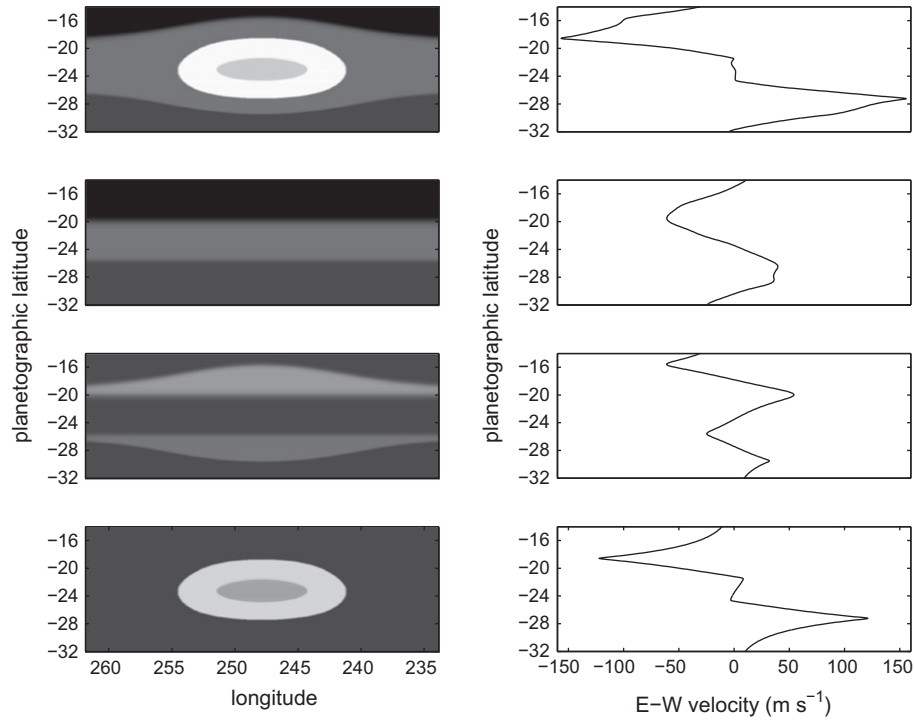


Fig. 16. Vortex–zonal flow interactions. Left column, from top row to bottom row: q or total PV from the best-fit model of the GRS; q^∞ or far-field PV; q^{INT} or interaction PV; and q^{GRS} or the PV of the vortex. A gray-scale color-map is used with white representing the most anti-cyclonic flow, and black representing the most cyclonic flow. The right column shows the corresponding east–west velocity produced by each PV along the north–south principal axis of the GRS.

equilibrium functions $q^\infty(y)$, $q^{GRS}(x,y)$ and $q(x,y)$, and then using the definition in Eq. (8). In general, equilibrium is only possible with a non-zero $q^{INT}(x,y)$. To understand the PV interaction from a physical point of view, consider the locations in latitude y of the PV jumps ΔQ_E and ΔQ_W as functions of longitude x . These locations for the flow around the GRS are the two streamlines shown as thick, white curves in Fig. 17. The velocity created by the PV anomaly of the GRS causes those streamlines to bend around the GRS, rather than intersect it. (The outer boundary of the GRS’s PV anomaly is also a streamline, and streamlines cannot intersect except at stagnation points where the velocity must be zero.) Fig. 16 shows that $q^{INT}(x,y)$ is created by the bending of the PV jumps of the zonal flow around the GRS. That is, $q^{INT}(x,y)$ is what needs to be added to the straight streamlines of the far-field zonal flow (second panel from top in Fig. 16) so that the zonal flow bends around the GRS.

Fig. 16 shows that q^{INT} consists of two compact regions of PV anomaly just north and south of the GRS. By definition, q^{INT} asymptotes to zero far from the GRS. For the GRS, $\Delta Q_E > 0$ and $\Delta Q_W < 0$, so the two patches of q^{INT} are both anti-cyclonic (counter-clockwise) like the GRS. The velocities created by the total PV and its three

components are shown on the right-hand side of Fig. 16. The velocity created by q^∞ embeds the GRS in anti-cyclonic shear; however, the velocity produced by the two anti-cyclones that make up q^{INT} embeds the GRS in a cyclonic shear, such that the total shear that the GRS feels from $q^\infty + q^{INT}$ is nearly zero. If the PV of the far-field zonal flow decreased monotonically from the north to south pole, then ΔQ_W would be non-negative. A positive ΔQ_W together with a positive ΔQ_E would make q^{INT} into a dipole with an anti-cyclonic patch south of the GRS and a cyclonic patch north of it. This dipole would not significantly reduce the shear in which the GRS is embedded, but rather produce a westward-going jet near the center of the GRS, which would make the GRS drift rapidly to the west. The consequences of the effects of the shear produced by q^{INT} are discussed in Section 8.

6. Physical results for the Oval BA

Table 3 shows that there were no changes in the best-fit parameters of Oval BA between 2000 and 2006 that were greater than

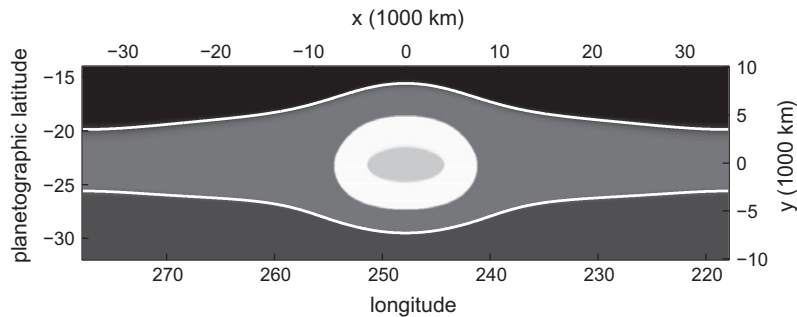


Fig. 17. PV of the best-fit model of the GRS as in Fig. 11, but here the thick, white streamlines indicate the locations of the PV jumps in the zonal component of the flow. The bending of the curves around the GRS is a result of the nonlinear interaction between the GRS and the zonal flow and is the reason the total PV of the flow cannot be modeled as a superposition of the PV of the GRS and the PV of the far-field zonal flow.

their uncertainties. The aspect ratio of the Oval’s PV anomaly has not changed, although the area of the PV anomaly has decreased by a small amount. However, it must be remembered that the calculations show that the Oval was probably not in equilibrium in 2000, so the area and other reported properties that are sensitive to the shape of the northern edge of the Oval BA in 2000 may have errors larger than the reported uncertainties. Table 3 also shows that the far-field PV near the latitudes of the Oval BA did not change, indicating that the bottom topography at these latitudes did not change.

Tables 2 and 3 show that there were no temporal changes in the Rossby deformation radius L_r that were greater than its uncertainties. However, the tables do show that L_r changes in latitude θ . The deformation radius is defined as $L_r \equiv NH/[f_n \sin(\theta)]$, where N is the Brunt–Väisälä frequency, f_n is the Coriolis parameter at the north pole, $H \equiv RT/g_j$ is the vertical pressure scale-height, T is the temperature, g_j is the gravity, and R is the gas constant of the atmosphere. All quantities are evaluated at the weather layer. Therefore,

$$N(\theta) = \frac{f_n g_j \sin(\theta) L_r(\theta)}{RT(\theta)}. \quad (9)$$

Assuming that values of $T(\theta)$ and its uncertainties are the cloud-top temperatures and uncertainties from Flasar (1986), T is the same at 33°S and at 23°S to within its observational uncertainty

of $\pm 1\%$. Assuming that g_j and R are independent of latitude, then H is also independent of latitude to within 1%. If we use $H = 20$ km as given in Gierasch et al. (2000) (the value of H has relatively negligible uncertainty) to compute the values of N , we get $N = 0.0158 \pm 0.0005 \text{ s}^{-1}$ and $N = 0.018 \pm 0.001 \text{ s}^{-1}$ at 23°S and 33°S respectively. Thus, we see that N is $15 \pm 10\%$ greater at 33°S than it is at 23°S.

6.1. Clouds, maximum velocities, stagnation points, and the location of the PV anomaly

Fig. 18 shows the streamlines of the best-fit flow from April 2006 in a frame translating with the Oval BA, superposed on an image of the Oval’s clouds from the HST observations in Table 1. The thick, black closed curve is the streamline that marks the outer boundary of the Oval’s PV anomaly. Like the GRS, the Oval BA has a PV anomaly with an area that is smaller (in fact, much smaller) than the area of the corresponding cloud cover. However, unlike the GRS, the Oval has a PV anomaly that is close to a stagnation point (north of the Oval near 29°S – see Fig. 19). At some locations, the streamline that feeds into this stagnation point is less than 1000 km from the PV boundary. Therefore perturbations of the flow could allow PV to be stripped from the Oval BA at the stagnation point. (See Humphreys and Marcus, 2007.) Unlike the GRS,

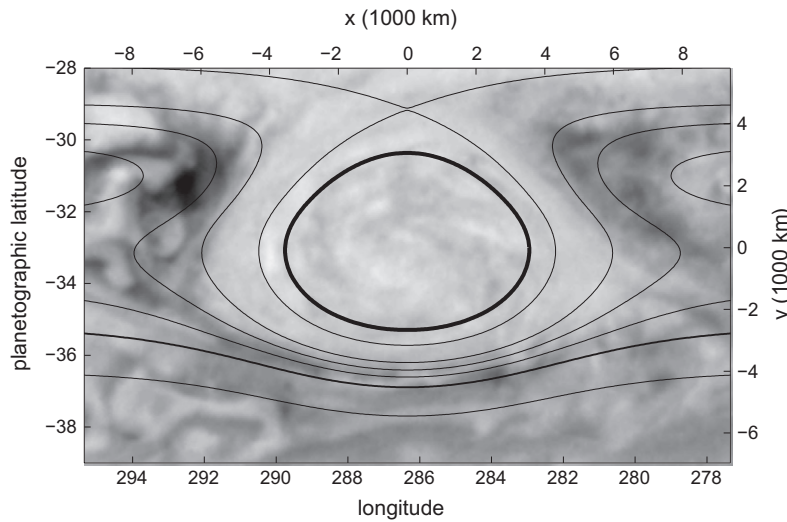


Fig. 18. Clouds and PV of the Oval BA. Image from HST (April 2006) of the Oval BA showing its cloud cover. Superposed are the streamlines of the best-fit velocity field. The thick, black closed streamline is the outer boundary of the PV anomaly of the Oval BA. Like the GRS (Fig. 10) the cloud cover is larger (especially on the northern side) than the PV anomaly.

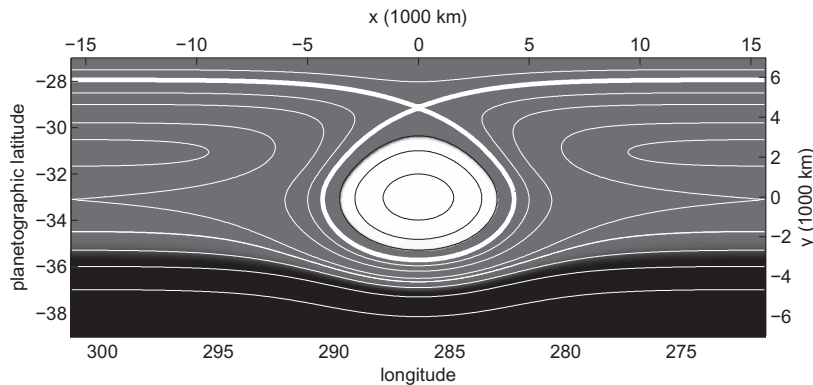


Fig. 19. Stagnation points and PV of the Oval BA. Streamlines for best-fit model of Oval BA using HST observations from April 2006 where the stagnation point north of the Oval BA is due to the crossing streamlines indicated with thick white lines. The value of the PV in the model is indicated with a gray-scale. The stagnation point is close to the PV anomaly of the Oval BA and therefore they can interact with each other. Unlike the GRS (see Fig. 11) which has two nearby stagnation points, the Oval BA has only one.

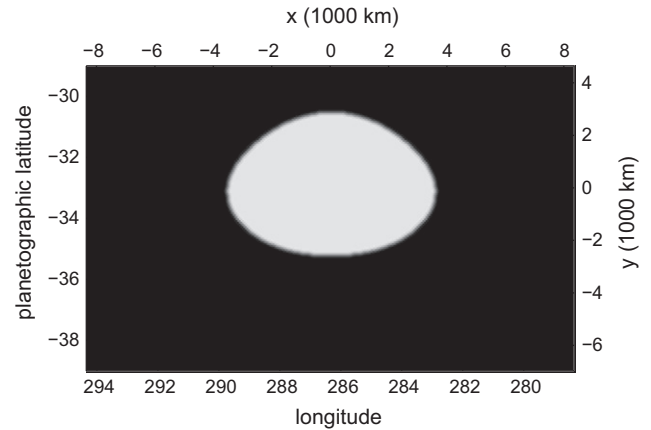
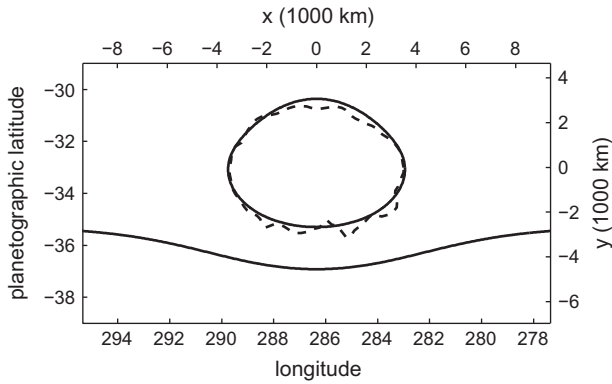


Fig. 20. Maximum velocities and PV of the Oval BA plotted as in Fig. 12. Unlike the GRS, the best-fit model of the Oval BA has only two contours of PV jumps (solid curves). The solid, closed contour denotes the outer boundary of the PV anomaly of the Oval BA and is nearly coincident with the maximum velocity contour (broken curve).

the Oval BA has only one nearby stagnation point, not two. Fig. 20 shows that the boundary of the PV anomaly of Oval BA is nearly coincident with the locus where the Oval has its local velocity maximum.

6.2. Ingredients of the Oval BA

The physics governing the Oval BA, like that of the GRS, can be illustrated by the effects of the different PV jumps in the best-fit model. Fig. 21 shows that when the models are constrained to have one PV jump in the Oval itself and none in the zonal flow (i.e., $q_2^{VOR} \equiv q_1^{VOR} \neq 0$ and $\Delta Q_W \equiv \Delta Q_E \equiv 0$), the best-fit of this restricted model reproduces the observed velocity everywhere along the east–west principal axis, including the core of the Oval. This is due to the fact that the Oval BA, unlike the GRS, is not hollow. Adding a second PV jump to the Oval BA (i.e., allowing $q_2^{VOR} \neq q_1^{VOR}$) does not improve the fit to the observations. Therefore, to simplify the presentation of our results in Table 2, we reported only the results of models that were constrained to have one PV jump for the Oval. Best-fit models that have one PV jump for the Oval and one PV jump for the zonal flow south of the Oval BA (i.e., $q_2^{VOR} \equiv q_1^{VOR} \neq 0$, $\Delta Q_W \equiv 0$, and $\Delta Q_E \neq 0$) give a slightly better match to the observed eastward-going jet stream along the north–south principal axis. The effect of adding the PV jump of ΔQ_E at y_E is not large because the magnitude of ΔQ_E is not large; it is less than half of the magnitude of the best-fit value of ΔQ_E that we found in the analysis of the GRS. PV and east–west velocities of this best-fit model are shown in Figs. 19 and 8b, respectively. We attempted to find models with two PV jumps in the zonal flow, one north of, and one south of the Oval BA (i.e., $\Delta Q_E \neq 0$ and $\Delta Q_W \neq 0$), but even for small values of ΔQ_W , our models did not converge for values of y_W near the Oval BA. The reason for this lack of convergence can be seen by comparing Fig. 11 for the GRS to Fig. 19 for the Oval BA. Contours of PV jumps must coincide with streamlines, and the streamlines of the far-field zonal component of the flow encircle the planet, or in our calculations are “open”, i.e., they begin on the left-hand boundary of the computational domain and continue to the right-hand boundary. Streamlines that are part of a vortex are “closed” and encircle the vortex. For the GRS, Fig. 11 shows that there are open or zonal streamlines both north and south of the GRS and that are close to the GRS. A PV jump could be placed on any of those streamlines, and the model would likely converge. In contrast, Fig. 19 shows the effect of the nearby stagnation point on the Oval BA. There are nearby, open, zonal streamlines south of the Oval that could support a PV anomaly, but there are no nearby, open zonal streamlines north of Oval BA. The closest open, zonal streamline

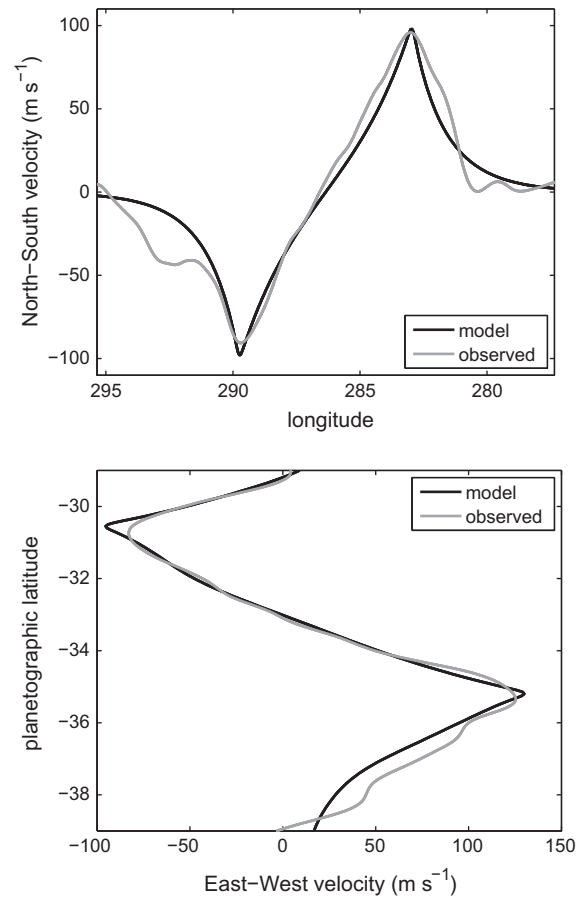


Fig. 21. Constrained best-fit model of the Oval BA. Here, the model’s PV is constrained to have no jumps in the zonal flow and only jump for the Oval itself (i.e., $\Delta Q_E \equiv \Delta Q_W \equiv 0$ and $q_2^{VOR} \equiv q_1^{VOR}$). As in Fig. 13, the PV of the constrained-best-fit model is in top panel; the north–south velocities of the model and observations are in the middle; and the east–west velocities are in the bottom. The observations and model are for the HST images of April 2006. The constrained model captures the locations and magnitudes of the north–south velocity peaks along the entire east–west principal axis. Unlike the GRS, the Oval BA is not hollow; a less constrained model with two, rather than one, PV jumps in the Oval BA does not give a better fit to the observed north–south velocity field. That is, when q_2^{VOR} is not constrained to be zero, its best-fit value is found to be very close to zero.

north of Oval BA is also north of the stagnation point, and placing a PV anomaly there (several deformation radii away from the boundary of the Oval) would have negligible effect on the Oval BA.

Thus, we set the best-fit value of ΔQ_W to be equal to zero, and the best-fit model of the Oval BA reported in Table 3 has only one jump in PV for the Oval and one jump in PV for the zonal flow.

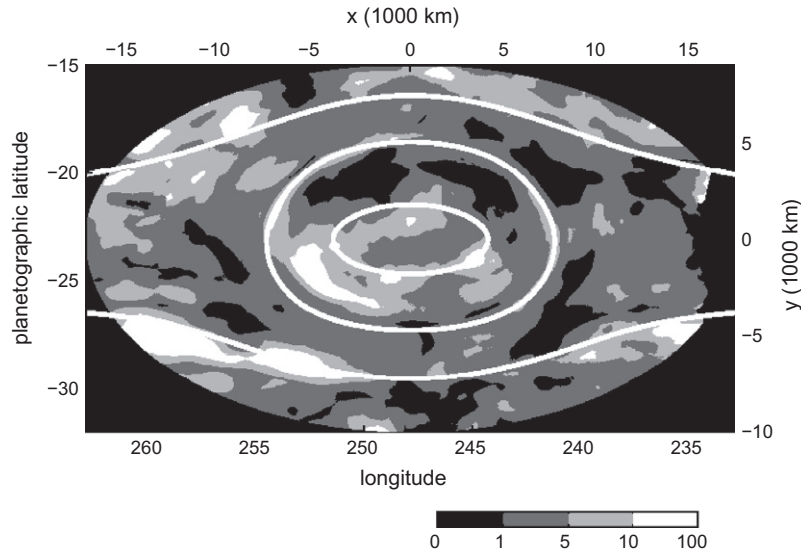


Fig. 22. Quality of model for the HST 2006 GRS. Each pixel (or i th grid point) is a measure of the difference between the ACCIV-extracted velocity and the best-fit model weighted by the uncertainty. The gray shading represents the value of $0.5 \left[|v_x^{(i)mod} - v_x^{(i)obs}| / \delta v_x^{obs}(i) + |v_y^{(i)mod} - v_y^{(i)obs}| / \delta v_y^{obs}(i) \right]$, where $v_x^{(i)obs}$ and $v_y^{(i)obs}$ are the x and y components of the observed velocities interpolated to the i th grid point (see Appendix), $v_x^{(i)mod}$ and $v_y^{(i)mod}$ are the components of the model velocity computed at the i th grid point, and $\delta v_x^{obs}(i)$ and $\delta v_y^{obs}(i)$ are the components of the scatter uncertainty interpolated to the i th grid point (see Appendix). The value of C_{vel} in Eq. (7) is the average over the individual pixel values within the oval shaped region shown in the figure (the black pixels in each corner of the rectangular domain demarcate the boundary of the oval shaped region). Because the observational uncertainty can be up to two times larger than the scatter uncertainty (see Section 2.1), locations where the pixel value is less than two indicate that the fit between model and observations is within the observational uncertainties. The four white curves are the contours of the model's PV jumps.

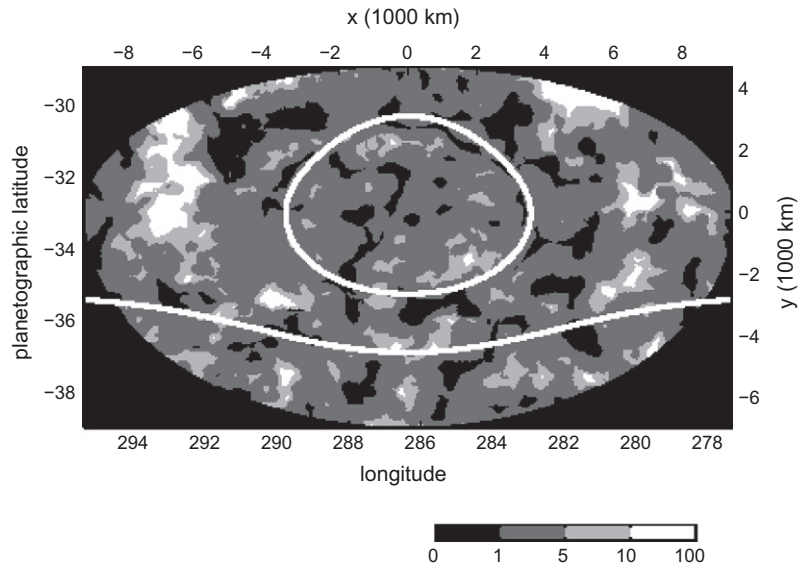


Fig. 23. Quality of model for the Oval BA. Each pixel is the difference between the ACCIV-extracted velocity and the best-fit model weighted by the uncertainty as in Fig. 22. The two white curves are the contours of the model's PV jumps.

The best-fit value of ΔQ_E for the Oval BA is positive (like the value of ΔQ_E of the GRS), indicating that the PV on the northern side of the jump at y_E is greater than that on the southern side.

7. Limitations of model

To see how the quality of the best-fit model varies within the computational domain, Figs. 22 and 23 show the spatial distribution of C_{vel} for best-fit models of HST data. For the best-fit model of the GRS, the largest discrepancies ($C_{vel} > 5$) occur near the eastward-going jet stream, in a region to the north–west of the GRS, and in a small region in the interior of the GRS near its southern

boundary. For the best-fit model of the Oval BA, the largest discrepancies occur outside the PV boundary of the Oval BA and are randomly located within the domain. A plot of the unweighted residual velocity vectors reveals spatial symmetries that suggest that the discrepancies in the interior of the GRS and near the eastward-going jet stream can be reduced with a steady-state solution that has a more complex PV distribution in these regions. However, the other discrepancies outside the PV boundary of the GRS and Oval BA do not show any spatial symmetry and are most likely due to small-scale time-dependent turbulence that cannot be captured within a 1.5-layer steady-state QG model, no matter how complex the distribution of piece-wise constant PV. The location

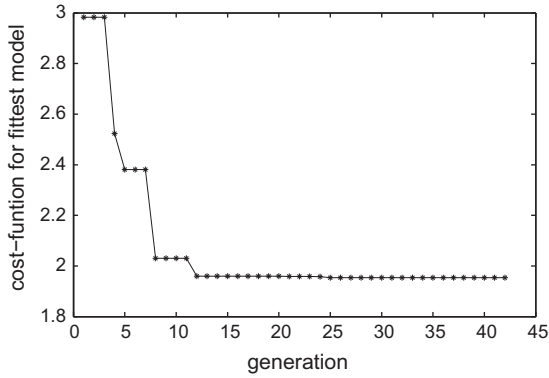


Fig. 24. Cost-function as function of generation. The figure shows the value of the cost-function $(C_{vel} + C_{area})/2$ for the fittest model in each generation.

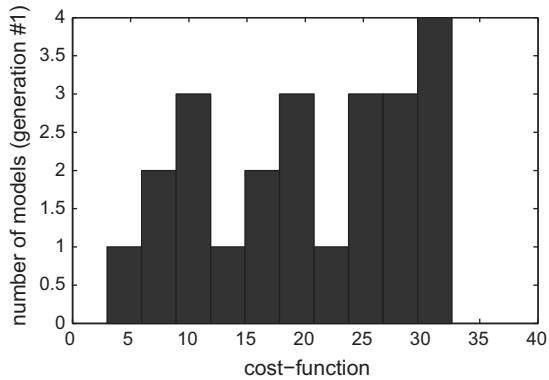


Fig. 25. Histogram of number of models as a function of the cost-function $(C_{vel} + C_{area})/2$. For the application of the genetic algorithm to the HST 2006 GRS velocity, the plot shows the distribution of the value of the cost-function for the first generation of models.

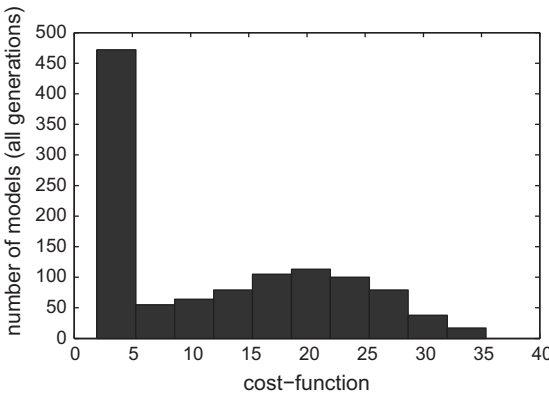


Fig. 26. Histogram of number of models as a function of the cost-function. As in Fig. 25 for the application of the genetic algorithm to the HST 2006 GRS velocity. This plot shows the distribution of the cost-function value for all of the models in all of the generations.

of these discrepancies outside the vortex boundary is consistent with known locations of time-dependence in the flow (example, the turbulent wake to the north–west of the GRS), and with the fact that vortices are known to suppress turbulence in their interiors. In any event, corrections to the model with characteristic velocities on the order of the RMS error of 15 m s^{-1} correspond to small perturbations to the PV of the best-fit equilibria, and should therefore not affect the main physical conclusions presented in this paper.

Reduction of the discrepancy further so that $C_{vel} \sim 2$ will no doubt require that we relax or remove some of the fundamental assumptions on which the model is based. For example, because the measured longitudinally-averaged far-field, zonal flow profile changes on a decadal time scale, it is certainly possible that by using different zonal profiles in the models we might obtain better fits to the observations and different “best-fit” parameter values. On the other hand because the 10-h/longitudinal variability of the zonal flow is of the same order, 11 m s^{-1} , as the decadal variability, it is also possible that the assumption of a steady, purely zonal far-field flow is not correct and that no model that uses this assumption will fit the observations better than the models presented here. We have not tried to include quantitatively the zonal variability into any of our measures of the fit between the model and observed velocities. However, based on our experiences with “trait-matching” (Shetty et al., 2007), we know that the parameter values for the magnitudes (q_1^{VOR} , q_2^{VOR}) and major diameters ($(D_x)_1$, $(D_x)_2$) of the PV anomalies of the GRS and Oval BA and of the Rossby deformation radius L_r are insensitive to the far-field zonal velocity profile. In contrast, the east–west velocities of the GRS and Oval BA are sensitive to the far-field zonal velocity profile, and the latitudes (y_E , y_W) and widths (δ_E , δ_W) of the PV jumps in our model are therefore sensitive to the far-field zonal velocity profile. However, the values of the PV jumps ΔQ_E and ΔQ_W of zonal flow are not. Those values strongly depend on the “roundness” of the GRS and Oval BA via the vortex–zone interaction sketched in Fig. 16; the values also depend somewhat weakly on the zonal shear averaged over all of the latitudes spanned by the vortices, but those average values appear to be stable over time (see Section 2.1). Thus despite the zonal variability, we are confident about our conclusion with respect to temporal changes (and lack of changes) in the areas and PV magnitudes of the GRS and Oval BA, with the change in L_r with latitude, and with the non-stair-casing of the PV jumps of the zonal flow.

The use of more complex equations that incorporate additional physics may also help reduce C_{vel} , although in Shetty (2008) we found that steady-state solutions of the Shallow-Water equations did not significantly improve the quality of fit. This suggests that the next level of improvement in fit will be obtained by incorporating three-dimensional effects and thermal effects that are not present in either the QG or Shallow-Water equations. In that case, the results presented here will help constrain feasible portions of parameter space. Even with just the 1.5-layer QG equations, the most accurate approach would be to let the PV for each computational grid point, the deformation radius L_r , and the bottom topography, all be unknown parameters. However, without any way of quickly computing equilibria for arbitrary PV distributions, we would have to solve the initial-value problem, and the optimization process would require a large amount of computational resources as already explained in Section 1, without necessarily providing more insight than our current model. Arguably, such an approach would provide no insight whatsoever because there would be no easy way to vary parameters and characterize the resulting physical consequences.

8. Conclusions and future work

The model that we use here is a physically motivated 11-parameter model that is a steady-state solution of the 1.5-layer QG equations when viewed in a frame translating with the vortex. Our algorithm for rapidly computing these models allowed us to efficiently and robustly search parameter space for best-fit models and their uncertainties. The models reproduce all the large-scale features of the flow, such as the GRS’s high-speed circumferential jet and quiescent core, with RMS errors of approximately 15 m s^{-1} for the GRS datasets. Reducing the error further will require a steady-state model with a more complex distribution of

PV, effectively increasing the number of free parameters. Reducing the error may also require a more accurate representation of the zonal flow and/or more complex equations that capture small-scale time-dependent effects. However, as argued earlier, we do not expect the incorporation of a more complex PV distribution or a more accurate zonal flow to affect the main physical results presented in this paper. We plan to verify these hypotheses in future work.

While almost all measured features of the vortices and zonal flows changed over time, very few of the changes were greater than the measured uncertainties as computed with a Monte Carlo boot-strap method. Without a reliable measure of uncertainty, it would have been easy to report many changes, when in fact few may have occurred. The QG best-fits and uncertainties support our previous conclusions (Asay-Davis et al., 2009): no dynamical properties of the Oval BA changed from 2000 when it was white to 2006 when it was red; the peak velocities of the GRS as well as the magnitudes of its PV have remained the same.

The most striking temporal change of the GRS is that its PV anomaly has become rounder (its aspect ratio has decreased by $17 \pm 8\%$) between 1996 and 2006. This change is consistent with our conclusion that the area of the PV anomaly of the GRS shrank by $18 \pm 4\%$. In stratified QG flows, vortices embedded in shearing zonal flows become rounder when their areas decrease. The closest stagnation point to the GRS is more than 7000 km from the outer boundary of its PV (Fig. 10). Therefore, it is unlikely that the area of the GRS's PV was stripped away at the stagnation point (although it is likely that some of the clouds covering the GRS are stripped away there). Humphreys and Marcus (2007) showed that the time-averaged equilibrium area of the PV anomaly of a vortex embedded in a set of alternating zonal winds is set by a balance between the dissipation rate of PV and the rate at which PV is appended to the vortex by mergers with smaller vortices. Thus, the shrinkage of the GRS could be due either to an increased dissipation or to “starvation” – the GRS is not merging with as many smaller vortices as it had in the past. A lack of mergers could be due to either a lack of supply of small vortices at the latitudes of the GRS or to an unknown dynamical effect that prevents mergers. We think the former is more likely than the latter because upheavals and other transient jovian behavior could easily affect the rate at which small vortices are created, but there is no obvious mechanism to prevent vortex mergers with the GRS.

Our results confirm for the first time in jovian vortices the well-established relation in laboratory vortices that the outer PV boundary coincides with the maximum circumferential velocities around the vortex. The best-fits results show that the outer boundaries of the PV anomalies in the GRS and Oval BA are nearly coincident with their maximum velocity loci. Therefore to a good approximation, the locations of the velocity extrema in Figs. 5–9 correspond to the outer boundaries of the PV anomalies of these jovian vortices.

Our analyses of the HST observations show that the Brunt-Väisälä frequency, which in the QG approximation is proportional to the average of the square root of the vertical stratification of entropy, is $15 \pm 10\%$ greater at 33°S than it is at 23°S . The uncertainty of this measurement is large, so it would be useful to verify this result in future work.

Some of the physical results from the best-fit analyses, which are difficult to establish with any other methodology, challenge our understanding of jovian atmospheric dynamics. For example, QG simulations on a β -plane with small-scale forcing show that alternating zonal flows are created by inverse cascades (Vallis and Maltrud, 1993). In those simulations the PV of the far-field zonal flow is piece-wise constant with jumps in PV only at the maxima of the eastward-going jet streams. Moreover, the PV monotonically decreases from north to south. Consistent with

these results, the best-fit analyses show that there are jumps in the PV at the eastward-going jet streams near the GRS and Oval BA. Both of the PV jumps show a decrease in PV from north to south. In addition, the westward-going jet stream that bends around the northern side of the Oval BA has no PV jump in our best-fit model. However, in contrast to expectations, the best-fit models show that the westward-going jet stream that bends around the northern side of the GRS has a large PV jump, and the sign of that jump shows an increase in PV from north to south. How this PV jump in the westward-going jet stream was created needs to be explained. In the future, it would be useful to analyze other jovian vortices to determine the magnitudes and signs of the PV jumps of other jet streams, especially of the westward going jet streams to determine whether the unexpected PV jump of the westward-going jet stream nearest to the GRS is unique.

Our best-fit analyses showed that the GRS was hollow with a PV minimum near its center, but that the Oval BA is not hollow. Future best-fit analyses should be carried out to determine whether there are other non-hollow jovian vortices. Our analysis shows that the tandem bending of the eastward-going jet stream and the westward-going jet stream with its PV with the unexpected sign around the GRS reduces the zonal shear at the vortex center. We have speculated (Shetty, 2008) that a reduction in zonal shear is necessary to stabilize hollow vortices. Therefore, if more hollow jovian vortices are found, it would be particularly important to determine if they are accompanied by westward jet streams with PV jumps and if so, what signs the PV jumps have.

Another interesting result from the modeling is that Figs. 11 and 19 show that in 2006 that the streamline and stagnation-point topology of the GRS and Oval BA differ. North of the GRS, there is an unimpeded westward-going flow arbitrarily close to the GRS. For the Oval BA, the stagnation point north of the Oval impedes the westward-going flow (that enters on the right-hand side of Fig. 19 between latitudes -33° and -31°). This flow cannot pass north of the Oval BA and is turned around to become an eastward-gong flow (that exits on the right-hand side of Fig. 19 between latitudes -31° and -28°). Whether the streamline topologies of the GRS or Oval BA change in time between the configurations shown in Figs. 11 and 19 is not known and should be pursued in future observations and modeling.

Acknowledgments

The HST observations presented here of jovian cloud images were made with the NASA/ESA Hubble Space Telescope. These observations are associated with HST Program GO/DD 10782, with support provided by NASA through a grant from the Space Telescope Science Institute, which is operated by the Association of Universities for Research in Astronomy, Inc., under NASA Contract NAS 5-26555. Analysis was supported by grants from the Planetary Atmospheres Program of NASA, the Berkeley-France fund, and the Astronomy and Astrophysics Program of NSF, with a computational allocation from the TeraGrid funded by NSF. We thank Ashwin Vasavada for sharing processed Galileo and Cassini imaging data. We thank Xylar S. Asay-Davis, Michael H. Wong, and Imke de Pater for the extracted velocity datasets.

Appendix A. Velocity uncertainties

A velocity vector is typically extracted from a tie-point pair in which a passively advecting feature (part of a cloud) is located in a first image (or mosaic) and then again at some time T later in a second image. To calculate the correlation uncertainty of a vector, all of the pixels of the first image are numerically advected with high precision forward for a time T using the extracted velocity field to create a synthetic second image. If the all of the vectors that

make up the velocity fields were exact, then the *second* image and *synthetic second* image would overlap exactly. In practice, there will be a displacement between the locations of a feature in the *second* image and the same feature in the *synthetic second* image. We define this displacement as the *correlation displacement* of the tie-point feature, and we define the velocity vector's *correlation uncertainty* to be the *correlation displacement* divided by T .

The ACCIV velocity field is interpolated to the computational grid points by computing a smooth surface that approximates the ACCIV velocity field in a least-squares sense as described in Asay-Davis et al. (2009). The *scatter uncertainties* are defined to be the difference between the approximating smooth surface and the ACCIV velocity field at the measurement locations. The *scatter uncertainties* are interpolated to the computational grid by taking the RMS average of all *scatter uncertainties* that lie within a distance r from the grid points. To determine an appropriate value for r , we increment r by small amounts until δv^{obs} converges in an L_2 -norm sense. In other words, we choose the smallest value of r required for statistical robustness. For all datasets, the value of r required for convergence was no greater than twice the effective resolution, and the average number of vectors in the RMS sum for each grid point was approximately 100.

Appendix B. Genetic algorithm

The genetic algorithm that we use to compute best-fit models is from Zohdi (2003) and consists of the following steps:

- (1) Initialize a *population* of N models by generating parameter sets at random from a uniform distribution on the parameter space of interest. Compute a model for each set of parameter values using the steady-state finding code.
- (2) Compute the cost-function for each model in the population. Sort models according to their cost.
- (3) Take the $2P$ *fittest* models, that is, the $2P$ models with the smallest cost and call them *parents*. Take the first two parent models and *breed* them to produce two *child* models. Then breed the next two parent models to produce two more child models and so on. Parameters of a child model are obtained by choosing a point at random between the parameter values of each parent. So if \mathbf{P}_1 and \mathbf{P}_2 are the parameter sets for two parents, then the i th parameter of a child is $t_i(P_1)_i + (1 - t_i)(P_2)_i$, where t_i is drawn uniformly at random from the interval $[0, 1]$.
- (4) Generate $N - 4P$ new random models or *mutants* (which help to remove false minima).
- (5) Initialize a new population of models composed of the $2P$ parents from the previous generation, their $2P$ children, and the $N - 4P$ mutants. This step marks the end of a *generation*. Return to Step 2.

We benchmarked the performance of the genetic algorithm using noisy synthetic velocity fields that were generated from the equilibrium-finding code for various choices of model parameters. In the benchmark runs, the genetic algorithm always converged to the model from which the velocity field was generated, which suggests that the best-fit model is unique. The uniqueness of the best-fit model as determined by the GA would be consistent with our “trait-matching” analysis (Shetty et al., 2007), where we showed that the model parameters could be determined uniquely from specific “traits” of the velocity field. For example, we found that the location of peak north–south velocity along the principal east–west axis uniquely determined the value of the east–west diameter $(D_x)_1$ of the vortex.

For runs of the GA that used an ACCIV-extracted velocity field, to reduce the likelihood of convergence to false minimum, we al-

ways run the GA for at least G generations, where G is the average number of generations that the GA required to converge to the minimum during benchmarking runs. After G generations have elapsed, we terminate the genetic algorithm as soon as the fittest model remains unchanged for 10 generations. After termination, we check that the fittest model is a true minimum using a star-search (Acton, 1990). The star-search is a derivative-free method for determining a local minimum by evaluating the cost-function at a cluster of points in parameter space, and then moving to the point where the cost-function is least. The cluster here consists of the starting point and two additional points for each coordinate axis, one on the positive and one on the negative side of the starting point. In cases where the fittest model was not a minimum, a couple of iterations of the star-search with small perturbations along each coordinate axis were sufficient to push the model to the minimum.

For the analysis of the GRS using the HST data, we chose N , the population size per generation, to be 48; the number of parents $2P$ to be 12, and the number of generations G to be 32. The bounds on the search were: $15,150 \text{ km} \leq (D_x)_1 \leq 15,650 \text{ km}$, $7000 \text{ km} \leq (D_x)_2 \leq 10,000 \text{ km}$, $1500 \text{ km} \leq L_r \leq 2500 \text{ km}$, $9.0 \times 10^{-5} \text{ s}^{-1} \leq q_1^{VOR} \leq 15.0 \times 10^{-5} \text{ s}^{-1}$, $5.0 \times 10^{-5} \text{ s}^{-1} \leq q_2^{VOR} \leq 10.0 \times 10^{-5} \text{ s}^{-1}$, $0.0 \leq \Delta Q_E \leq 10.0 \times 10^{-5} \text{ s}^{-1}$, $-10.0 \times 10^{-5} \text{ s}^{-1} \leq \Delta Q_W \leq 0.0$, $-27^\circ \leq y_E \leq -25^\circ$, $-21^\circ \leq y_W \leq -19^\circ$, $56 \text{ km} \leq \delta_E \leq 560 \text{ km}$, and $560 \text{ km} \leq \delta_W \leq 1120 \text{ km}$. For the analysis of the Oval BA using the HST data, we chose $N=24$, $2P=6$, and $G=32$. The bounds on the search were: $6800 \text{ km} \leq (D_x)_1 \leq 7200 \text{ km}$, $1000 \text{ km} \leq L_r \leq 2500 \text{ km}$, $5.0 \times 10^{-5} \text{ s}^{-1} \leq q_1^{VOR} \leq 2.0 \times 10^{-4} \text{ s}^{-1}$, $0.0 \leq \Delta Q_E \leq 10.0 \times 10^{-5} \text{ s}^{-1}$, $-38^\circ \leq y_E \leq -34^\circ$, and $58 \text{ km} \leq \delta_E \leq 580 \text{ km}$. The GA runs for the bounds given above sampled approximately 2000 models to determine the best-fit model. However, to check for the presence of multiple minima, we also ran cases with larger bounds on the parameters, or in different regions of parameter space, and the total number of models sampled over all these runs was on the order of 10,000.

For the best-fit model of the GRS using the HST 2006 velocities, Fig. 25 shows how the cost-function $(C_{vel} + C_{area})/2$ varies for the models in the first generation. The total number of models in the histogram is less than N because not every set of parameter values produces a steady-state model like the one shown in Fig. 4. Fig. 26 shows a histogram of how the cost-function varies for the models computed over all generations. Fig. 24 shows the evolution of $(C_{vel} + C_{area})/2$ for the fittest model in each generation. A plot in the 11-dimensional parameter space of the locations of the models that had values of C close to the minimum value shows that there is a unique location, rather than multiple locations, where the points are clustered. The size of the scatter of the points in the 11-dimensional space is approximately equal to the uncertainties in the parameter values found by the Monte Carlo boot-strap method listed in Tables 2 and 3.

References

- Acton, F.S., 1990. Numerical Methods that Work. Mathematical Association of America.
- Asay-Davis, X.S., Marcus, P.S., Wong, M., de Pater, I., 2009. Jupiter's shrinking Great Red Spot and steady Oval BA: Velocity measurements with the 'Advection Corrected Correlation Image Velocimetry' automated cloud tracking method. Icarus 203, 164–188.
- Asay-Davis, X.S., Wong, M., Marcus, P.S., de Pater, I., 2010. Changes in Jupiter's zonal wind profile from 1979 to 2008. Icarus, submitted for publication.
- Cho, J.Y.-K., de la Torre Juarez, M., Ingersoll, A.P., Dritschel, D.G., 2001. High-resolution, three-dimensional model of Jupiter's Great Red Spot. J. Geophys. Res. 106 (15), 5099–5106.
- Cho, J.Y.-K., Polvani, L.M., 1996. The emergence of jets and vortices in freely evolving, shallow water turbulence on a sphere. Phys. Fluids 8, 1531–1552.
- Dowling, T.E., Ingersoll, A.P., 1989. Jupiter's Great Red Spot as a shallow water system. J. Atmos. Sci. 46 (21), 3256–3278.
- Fincham, A.M., Spedding, G.R., 1997. Low cost, high resolution DPIV for measurement of turbulent fluid flow. Exp. Fluids 23, 449–462.

- Flasar, F.M., 1986. Global dynamics and thermal structure of Jupiter's atmosphere. *Icarus* 65, 280–303.
- García-Melendo, E., Sánchez-Lavega, A., 2001. A study of the stability of jovian zonal winds from HST images: 1995–2000. *Icarus* 152, 316–330.
- García-Melendo, E., Sánchez-Lavega, A., Hueso, R., 2007. Numerical models of Saturn's long-lived anticyclones. *Icarus* 191, 665–677.
- Gierasch, P.J., Ingersoll, A.P., Banfield, D., Ewald, S.P., Helfenstein, P., Simon-Miller, A., Vasavada, A., Breneman, H.H., Senske, D.A., and Galileo Imaging Team, 2000. Observation of moist convection in Jupiter's atmosphere. *Nature* 403, 628–630.
- Hawley, J.F., Balbus, S.A., 1992. A powerful local shear instability in weakly magnetized disks. III – Long-term evolution in a shearing sheet. *Astrophys. J.*, Part 1 400, 595–609.
- Humphreys, T., Marcus, P.S., 2007. Vortex street dynamics: The selection mechanism for the areas and locations of Jupiter's vortices. *J. Atmos. Sci.* 64, 1318–1333.
- Legarreta, J., Sánchez-Lavega, A., 2008. Vertical structure of Jupiter's troposphere from nonlinear simulations of long-lived vortices. *Icarus* 196, 184–201.
- Limaye, S.S., 1986. Jupiter: New estimates of the mean zonal flow at the cloud level. *Icarus* 65, 335–352.
- Marcus, P.S., 1993. Jupiter's Great Red Spot and other vortices. *Rev. Astron. Astrophys.* 31, 523–573.
- Marcus, P.S., Kundu, T., Lee, C., 2000. Vortex dynamics and zonal flows. *Phys. Plasmas* 7, 1630–1640.
- McIntyre, M.E., 2008. Potential-vorticity inversion and the wave-turbulence jigsaw: Some recent clarifications. *Adv. Geosci.* 15, 47–56.
- Morales-Juberías, R., Dowling, T.E., 2005. Simulations of high-latitude spots on Jupiter: Constraints on vortex strength and the deep wind. *Planet. Space Sci.* 53, 1221–1233.
- Morales-Juberías, R., Sánchez-Lavega, A., Dowling, T.E., 2003. EPIC simulations of the merger of Jupiter's White Ovals BE and FA: Altitude-dependent behavior. *Icarus* 166, 63–74.
- Pedlosky, J., 1987. *Geophysical Fluid Dynamics*. Springer-Verlag, New York.
- Porco, C.C., and 23 colleagues, 2003. Cassini imaging of Jupiter's atmosphere, satellites, and rings. *Science* 299, 1541–1547.
- Press, W.H., Flannery, B.P., Teukolsky, S.A., Vetterling, W.T., 1988. *Numerical Recipes in C: The Art of Scientific Computing*. Cambridge University Press, New York, NY, USA. ISBN 0-521-35465-X.
- Read, P.L., Gierasch, P.J., Conrath, B.J., Simon-Miller, A., Fouchet, T., Yamazaki, Y.H., 2006. Mapping potential-vorticity dynamics on Jupiter. I: Zonal-mean circulation from Cassini and Voyager 1 data. *Q. J. R. Meteor. Soc.* 132, 1577–1603.
- Shetty, S., 2008. *Formulation and Solution of the Inverse Problem for Jupiter's Atmospheric Vortices*. PhD thesis, University of California at Berkeley.
- Shetty, S., Asay-Davis, X.S., Marcus, P.S., 2007. On the interaction of Jupiter's Great Red Spot and zonal jet streams. *J. Atmos. Sci.* 64, 4432–4444.
- Simon, A.A., 1999. The structure and temporal stability of Jupiter's zonal winds: A study of the North Tropical Region. *Icarus* 141, 29–39.
- Simon, A.A., Beebe, R.F., 1996. Jovian tropospheric features—wind field, morphology, and motion of long-lived systems. *Icarus* 121, 319–330.
- Simon-Miller, A.A., Gierasch, P.J., Beebe, R.F., Conrath, B., Flasar, F.M., Achterberg, R.K., and the Cassini CIRS Team, 2002. New observational results concerning Jupiter's Great Red Spot. *Icarus* 158, 249–266.
- Spalart, P., 1998. Aircraft trailing wake vortices. *Annu. Rev. Fluid Mech.* 30, 107–138.
- Vallis, G.K., Maltrud, M.E., 1993. Generation of mean flows and jets on a beta plane and over topography. *J. Phys. Oceanogr.* 23, 1346–1362.
- Van Buskirk, R.D., 1991. *Quasigeostrophic Vortices in Zonal Shear*. PhD thesis, Harvard University.
- Zohdi, T.I., 2003. Genetic design of solids possessing a random-particulate microstructure. *Philos. Trans. R. Soc. A: Math. Phys. Eng. Sci.* 361, 1021–1043.